Applied Mathematical Modelling 109 (2022) 161–185

Contents lists available at ScienceDirect

Applied Mathematical Modelling

journal homepage: www.elsevier.com/locate/apm

An isogeometric boundary element method for heat transfer problems of multiscale structures in electronic packaging with arbitrary heat sources

Yanpeng Gong[a,b,*], Fei Qin[a,b], Chunying Dong[c], Jon Trevelyan[d]

[a] Institute of Electronics Packaging Technology and Reliability, Faculty of Materials and Manufacturing, Beijing University of Technology, Beijing 100124, China
[b] Beijing Key Laboratory of Advanced Manufacturing Technology, Faculty of Materials and Manufacturing, Beijing University of Technology, Beijing 100124, China
[c] Department of Mechanics, School of Aerospace Engineering, Beijing Institute of Technology, Beijing 100081, China
[d] Department of Engineering, Durham University, Durham DH1 3LE, UK

ARTICLE INFO

Article history:
Received 14 June 2021
Revised 16 March 2022
Accepted 31 March 2022
Available online 9 April 2022

Keywords:
Boundary element method
Isogeometric analysis
Heat transfer problems
Radial integral method
Multiscale problems

ABSTRACT

We present an isogeometric boundary element method (IGABEM) capable of studying heat transfer problems for multiscale structures in electronic packaging problems. This method offers a number of key improvements compared with current analysis methods available for electronic packaging problems. The method benefits from the accuracy, computational efficiency and CAD integration that have consistently been shown as features of the IGA-BEM. In addition, the current method can efficiently evaluate the nearly singular integrals caused by multiscale structures, owing to the use of a proposed hybrid integration scheme. By changing a tolerance, the scheme enables engineers to achieve any desired balance between accuracy and computational efficiency as may be appropriate to the situation. To study heat transfer problems with an arbitrary heat source, the radial integral method is used to transform the domain integral to an equivalent boundary integral. Numerical results are compared with available analytical solutions and finite element solutions and demonstrate the effectiveness of the proposed approach.

1. Introduction

The temperature control in electronic packaging plays a key role in numerous applications, to avoid overheating and hardware failure. However, from thermal perspective, all power semiconductor devices act as heat sources dissipating power through electronic packages into printed circuit boards (PCB) and heat sinks. Due to high capability of heat transfer, good temperature uniformity, and no power consumption, heat pipes or cooling fins are widely used for heat dissipation of electronic components [1,2]. In recent years, the size of semiconductor components has typically been reducing. As a result, the numerical modeling of semiconductor structures becomes highly challenging, particularly where both small structures and large structures interact. For these models with complex and multiscale structures, very refined meshes can be needed to

* Corresponding author at: Institute of Electronics Packaging Technology and Reliability, Faculty of Materials and Manufacturing, Beijing University of Technology, Beijing 100124, China.
E-mail address: yanpeng.gong@bjut.edu.cn (Y. Gong).

https://doi.org/10.1016/j.apm.2022.03.047
0307-904X/

obtain the required accuracy, which results in a heavy burden on the computational resources [3]. In order to tackle this problem, many researchers have proposed techniques for the numerical simulation of multiscale structures in electronic packaging [4,5]. In this work, we will develop a scheme to consider some problems, commonly found in electronic packaging, of odd shaped heat sources active on planar structures like circuit boards subjected to heat sources of arbitrary shape as imposed by hot components and connections.

In 2005, to bridge the gap between CAD and computer aided engineering (CAE), Hughes et al. [6] proposed the concept of isogeometric analysis (IGA) in which the Non-Uniform Rational B-Splines (NURBS) basis functions are used to describe a geometric model. Since the same basis functions are used to represent the geometry of models in CAD and IGA, this analysis formulation has been attracting attention as a promising method for integrating CAD and CAE. In addition, the meshing process for FEM is greatly simplified in the numerical analysis by using IGA. With these benefits, many advancements in IGA have been achieved. Recently, by using the isogeometric concept for dealing with the higher continuity conditions required for primal variational formulation of the flexoelectric coupled system of PDEs, López et al. [7] proposed a phase-field based method for shape and topology optimization of flexoelectric micro-structures. An isogeometric approach in three dimensions for nonlinear problems in solid mechanics and structural dynamics was presented in Chasapi et al. [8]. In [9], two efficient quadrature rules, reduced Gauss quadrature and Gauss-Greville quadrature, for isogeometric analysis are developed. Both the proposed quadrature rules involve many fewer quadrature points than the full Gauss quadrature rule and avoid negative quadrature weights for arbitrary knot vectors. In [10], the authors proposed a method of IGA-suitable planar parameterization based on patch structure simplification of the closed-form polysquare. In [11], Videla et al. demonstrate the applications of PHT-splines in the framework of Geometry Independent Field approximaTion (GIFT) for problems of time-harmonic acoustics modeled by the Helmholtz equation. Then, the GIFT scheme is extended to a plane-wave Partition of Unity enriched GIFT in Jansari et al. [12]. In [13], an adaptive extended isogeometric analysis (XIGA) is used to study the shakedown problems with holes. Based on the IGA and scaled boundary element method Zang et al. [14] developed a numerical scheme to solve the static bending and free vibration problems of functionally graded material plates. Actually, IGA has attracted a large research community and been successfully applied in elasticity problems [15–17], electromagnetics [18–20], fluids problems [21,22], accoustic problems [23,24], wave problems [25], contact problems [26], vibration analysis [27–29], cracks [30–34], optimization problems [35–37], material uncertainty [38], thermal buckling [39], poroelastic material [40], etc. Since the initial IGA was based on NURBS [6] which contains a tensor product form, the uniform NURBS-based refinement scheme is difficult to capture local features of interest. In order to ameliorate this difficulty, the method has been extended to T-splines [41,42], THB-splines [43], hierarchical B-splines (HB) [15], LR-splines [44], hierarchical box splines [45] and Powell–Sabin B-splines [46].

With the advantages of boundary-only descretisation, high solution accuracy and ability to model discontinuous functions, BEM is a very promising method for the analysis of complex and multiscale structures in electronic packaging problems [47]. Due to the fact that the boundary element method (BEM) and CAD rely on a surface definition, they match each other well. Therefore, based on the isogeometric analysis (IGA) concept, the isogeometric boundary element method (IGABEM) was later presented [48]. The main idea of isogeometric formulations is replacing the piecewise polynomial approximation of geometries and physical quantities by an approximation formed in a space of Non-Uniform Rational B-Spline (NURBS) basis functions. Therefore, the IGABEM integrates the advantages of IGA and the merits of BEM. The advantages are (i) the use of an exact geometric representation; (ii) the reduction of the dimensionality of considered problem by one; (iii) the improved convergence properties of the solution; (iv) high accuracy for many engineering problems. It should be pointed out that both the BEM and CAD rely on a surface definition, so the BEM can be seen as a more natural numerical method than the finite element method (FEM) for the tight integration of the isogeometric analysis and CAD modeling. The IGABEM framework has been used in various areas including elastostatics [49–51], acoustics [52], heat conduction [53], topology optimization [54–57], liquid sloshing [58], fracture [59,60], potential problems [61], and underground excavations [62].

As we will show in this article, the IGABEM is an attractive numerical method for the analysis of multiscale structures for electronic packaging [63]. The geometric properties of multiscale structures or quite convoluted heat sources (e.g. from components and wiring on a printed circuit board) commonly found in electronic systems can be accurately represented with a small number of boundary elements, which naturally reduces the number of degree of freedom (DOF) used in calculation. Quantities along the thickness direction of thin structures can be calculated accurately.

The implementation of the IGABEM introduces some challenges when solving multiscale structures in electronic packaging problems. One of the major problems is the accurate evaluation of the different boundary integrals that arise. It is well known that BEM implementations involve singular integrals, but also that the nearly singular integrals (where the collocation point is close to, but not on, the element being integrated) can often cause more difficulties than the singular cases. When applied to multiscale structures, a large number of nearly singular integrals will be required, caused by the presence of elements having very different dimensions. Thus, it will be important to develop methods capable of integrating nearly singular kernels in a robust and computationally efficient manner. To date, many schemes have been presented to evaluate nearly singular integrals in both the conventional BEM and IGABEM. A detailed review of evaluation techniques of nearly singular integrals for conventional BEM can be found in Gu et al. [64]. In recent years, with the development of IGABEM as a preferred approach, some integration schemes for nearly singular integrals in IGABEM have emerged. Gong et al. [65] illustrate the necessity of evaluating the near singular integral in IGABEM, and use the exponential transformation method to remove or weaken the near singularities in potential problems. In [66], the nearly singular integrals are computed by sinh-

transformation method. In [67], a semianalytical method is presented to evaluate the nearly singular integrals in IGABEM. Recently, a hybrid nearly singular integration method is given in Gong et al. [68,69], in the study of coated structures, that is capable of producing accurate and efficient solutions for thin sections. Inspired by the idea in Gong et al. [68,69] and the exponential transformation method in Gong et al. [65], we will develop an efficient scheme to study heat transfer problems for multiscale structures with heat sources.

In the analysis of multiscale structures using the IGABEM, the geometry of the numerical model can be described accurately using a smaller number of elements than in classical BEM. Indeed many geometric constructions are represented exactly using NURBS. Thus, the corresponding geometric area of a knot span (which can be seen as the IGABEM interpretation of a boundary element in BEM) may be considerably larger than that of traditional method. To obtain accurate results, a higher order of Gauss integration should be used, and the computational cost will increase rapidly if a fixed order of Gauss integration is used. Based on the upper bound of the relative error of the Gaussian quadrature formula for traditional BEM, Gao and Davies [70] presented an adaptive integration method. In [71], an IGABEM using an adaptive integration scheme is developed and applied to 3D potential problems. In this method, the isogeometric element is subdivided into sub-elements to avoid using excessively high Gauss order according to Davies and Bu's criterion [72]. In the current work, the adaptive integral scheme will be adopted to study multiscale structures.

The accurate determination of temperature distributions is an important problem in multiscale semiconductor structures subjected to heat sources [73]. The implementation of the BEM presents a further challenge when solving heat transfer problems with distributed heat sources, because domain integrals arise in the resulting integral equations alongside the normal boundary integrals. The evaluation of domain integrals is typically more time consuming than for boundary integrals. Although the domain integrals can be directly computed by discretizing the domain into internal cells, the method eliminates one key advantage of the BEM in which, otherwise, only the boundary of the problem needs to be discretized into elements [74]. Therefore, many schemes have been presented to transform the domain integrals into equivalent boundary integrals, e.g. the dual reciprocity method [75], the multiple reciprocity method [76] and the radial integration method (RIM) [77]. A detailed review of such transformation schemes can be found in Gao [78]. The radial integration method proposed by Gao [77] is based on a purely mathematical technique, and can be adopted in the current IGABEM work.

In this work, we develop an IGABEM algorithm for multiscale structures with arbitrary heat sources. A hybrid integration scheme, that combines the exponential transformation method and adaptive integral method, is presented to deal with the nearly singular integrals caused by the different sizes of the structural component parts. An important feature of the scheme is that the integration method is tuned to deliver results of satisfactory accuracy in the optimal computation time. In the computation, when the source point is very close to the element being integrated (the distance being considered relative to the element size) the hybrid integration scheme will be used, and for source points at a larger distance, the adaptive integral method will be used. Here, the RIM is used to evaluate the domain integrals caused by the heat source with arbitrary geometries, including some complex geometries or thin sections.

We are interpreting multiscale modeling as the analysis of models containing geometric features at different length scales. The cooling fins in the convection examples are a good illustration of this. These geometries present major challenges to FEM practitioners, yet IGABEM gives us an attractive numerical alternative. The geometric properties of multilevel interconnected structures can be accurately represented with a small number of boundary elements, which naturally reduces the DOF used in calculation, because many of the FEM meshing problems arise due to the volumetric meshing that BEM avoids. However, the implementation of the IGABEM introduces some challenges when solving such structures in electronic packaging problems because of the nearly singular integrals that arise. In this work, we developed an IGABEM to solve these problems by proposing an efficient and robust scheme to evaluate the nearly singular integrals as well as the domain integrals caused by heat sources.

This paper is organized as follows. In Section 2, an overview of the BEM and IGABEM formulation is given. We present our integration scheme for multiscale geometry structures in Section 3. Section 4 introduces the implementation of the current isogeometric boundary element method. In Section 5, we demonstrate the effectiveness of the new IGABEM scheme through several numerical examples. Finally, we present the conclusions for our work.

2. Boundary element method and isogeometric boundary element method

2.1. Fundamental formulations

Consider a structure occupying a continuous physical domain, $\Omega \in \mathbb{R}^2$, with closed boundary Γ. The governing equation of steady-state heat transfer is given by

$$\nabla^2 u(\mathbf{x}) + b(\mathbf{x}) = 0 \tag{1}$$

where $\mathbf{x} = (x_1, x_2) \in \Omega$, the non homogeneous term $b(\mathbf{x})$ denotes internal heat sources, and $u(\mathbf{x})$ denotes temperature at point $\mathbf{x}$. For heat transfer problems, the flux density q_i in direction x_i is defined as $q_i = -k\partial u/\partial x_i$. The quantity of heat passing through a unit area can be described by normal flux density q, defined as

$$q = q_i n_i = -k u_{,i} n_i \tag{2}$$

in which k is the thermal conductivity, n_i ($i = 1, 2$ for 2D problems) are the components of the unit outward normal vector $\mathbf{n}$, $u_{,i}$ denotes the differentiation of temperature with respect to the ith component of the coordinate, x_i, i.e.

$$u_{,i} = \frac{\partial u}{\partial x_i} \tag{3}$$

and the Einstein summation convention is adopted. Eq. (1) can be solved subject to a set of boundary conditions taken from the following forms:

$$u = \bar{u} \text{ on } \Gamma_{\bar{u}} \subset \Gamma \tag{4}$$

$$q = \bar{q} \text{ on } \Gamma_{\bar{q}} \subset \Gamma \tag{5}$$

where $\bar{u}$ and $\bar{q}$ are known temperature and flux density; $\Gamma_{\bar{u}}$ and $\Gamma_{\bar{q}}$ represent the parts of Γ over which temperature and flux density are prescribed. It should be noted that $\Gamma_{\bar{u}} \cap \Gamma_{\bar{q}} = \oslash$ and $\Gamma_{\bar{u}} \cup \Gamma_{\bar{q}} = \Gamma$.

For a heat transfer problem, the corresponding boundary-domain integral equation can be written as

$$c(\mathbf{y})u(\mathbf{y}) + \int_\Gamma Q(\mathbf{y}, \mathbf{x})u(\mathbf{x})d\Gamma(\mathbf{x}) = \int_\Gamma U(\mathbf{y}, \mathbf{x})q(\mathbf{x})d\Gamma(\mathbf{x}) + \int_\Omega b(\mathbf{x}')U(\mathbf{y}, \mathbf{x}')d\Omega(\mathbf{x}') \tag{6}$$

where $\mathbf{x}' \in \Omega$. $\mathbf{y} = (y_1, y_2) \in \Gamma$ and $\mathbf{x} = (x_1, x_2) \in \Gamma$ are the source point and field point, respectively. In the collocation form of the BEM as used in this paper, a source point $\mathbf{y}$ also represents a collocation point. $U(\mathbf{y}, \mathbf{x})$ denotes the temperature fundamental solutions and $Q(\mathbf{y}, \mathbf{x})$ is its normal derivative. For 2D heat transfer problems, U and Q are known and can be expressed as

$$U(\mathbf{y}, \mathbf{x}) = -\frac{1}{2\pi} \ln r, \tag{7}$$

$$Q(\mathbf{y}, \mathbf{x}) = \frac{\partial U(\mathbf{y}, \mathbf{x})}{\partial \mathbf{n}(\mathbf{x})} = \frac{\partial U(\mathbf{y}, \mathbf{x})}{\partial r} \frac{\partial r}{\partial \mathbf{n}(\mathbf{x})} \tag{8}$$

in which $r = r(\mathbf{y}, \mathbf{x}) = |\mathbf{x} - \mathbf{y}|$ represents the distance between source point $\mathbf{y}$ and field point $\mathbf{x}$.

2.2. Introduction to B-splines and NURBS basis

In this work, we focus on heat transfer problems with arbitrary heat sources in multiscale structures. Different integrals including domain integrals and nearly singular boundary integrals will be evaluated by some specially developed integration schemes. In order to facilitate presentation of these schemes, a brief introduction of B-splines and NURBS basis functions is first given in this section.

The B-spline basis functions of degree $p = 0$ can be defined recursively with piecewise constants

$$N_{a,0}(\xi) = \begin{cases} 1, & \text{if } \xi_a \le \xi < \xi_{a+1} \\ 0, & \text{otherwise,} \end{cases} \tag{9}$$

where ξ_a is a knot in the knot vector Θ which contains non-decreasing values

$$\Theta = \left\{\xi_1, \xi_2, ..., \xi_{n+p+1}\right\}, \ \xi_a \in \mathbb{R} \tag{10}$$

in which a is the knot index; n represents the number of basis functions. Then, B-spline basis functions of degree $p \neq 0$ are defined by

$$N_{a,p}(\xi) = \frac{\xi - \xi_a}{\xi_{a+p} - \xi_a} N_{a,p-1}(\xi) + \frac{\xi_{a+p+1} - \xi}{\xi_{a+p+1} - \xi_{a+1}} N_{a+1,p-1}(\xi), \tag{11}$$

where $p = 1, 2, \ldots$ and $\xi \in [\xi_a, \xi_{a+1}]$.

The basis functions describing a NURBS of degree p are weighted forms of the B-spline basis functions, and are defined as

$$R_{a,p}(\xi) = \frac{N_{a,p}(\xi)w_a}{\sum_{i=1}^{p+1} N_{i,p}(\xi)w_i} \tag{12}$$

where w_a is a weight associated with the control point $\mathbf{P}_a \in \mathbb{R}^2$.

The derivatives of NURBS basis functions may be written as Simpson et al. [49]

$$\frac{d}{d\xi} R_{i,p}(\xi) = \omega_i \frac{W(\xi)N'_{i,p}(\xi) - W'(\xi)N_{i,p}(\xi)}{(W(\xi))^2} \tag{13}$$

where $N_{i,p}(\xi)$ is the B-spline basis function given in Eqs. (9) and (11), $N'_{i,p}(\xi) = \frac{d}{d\xi} N_{i,p}(\xi)$, and $W'(\xi) = \sum_{j=1}^{n} N'_{j,p}(\xi)\omega_j$.

The higher-order derivatives of the rational function can be expressed in terms of lower-order derivatives as Simpson et al. [49]

$$\frac{d^k}{d\xi^k}R_{i,p}(\xi)=\frac{A_i^{(k)}(\xi)-\sum_{b=1}^{k}\binom{k}{b}W^{(b)}(\xi)\frac{d^{(k-b)}}{d\xi^{(k-b)}}R_{i,p}(\xi)}{W(\xi)} \tag{14}$$

where $\binom{k}{b}=\frac{k!}{b!(k-b)!}$, $A_i^{(k)}(\xi)=\omega_i\frac{d^k}{d\xi^k}N_{i,p}(\xi)$ and $W^{(b)}(\xi)=\frac{d^b}{d\xi^b}W(\xi)$.

2.3. Description of boundary geometry

For the IGABEM, the geometry of the numerical model is described by NURBS basis functions. Given a control set $\mathbf{P}_a$, $a=1,2,\ldots,n$, and a knot vector Θ (shown in Eq. (10)), a NURBS curve is defined using

$$C(x,y)=\sum_{i=1}^{n}R_{i,p}(\xi)\mathbf{P}_i \tag{15}$$

where $R_{i,p}(\xi)$ is a NURBS basis function of degree p; n is the number of basis function. It should be noted that when all the weights are same values, the NURBS curve will degenerate to a B-spline curve.

For a single 'knot span', which plays the role of 'element' in conventional BEM, there are $p+1$ non-zero basis functions. Then the mapping from the parameter space to physical space can be expressed as

$$\mathbf{x}(\xi)=\sum_{i=1}^{p+1}R_{i,p}(\xi)\mathbf{P}_i \tag{16}$$

2.4. Analysis of different integration methods for a single knot span

In this section we will compare the relative error and CPU time of several integral methods for the computation of nearly singular integrals, including Gauss–Legendre [68,79], adaptive integral method [68,71] and transformation method [65]. The main feature of the adaptive integral method is that the method can deliver high accuracy (with upper bound of relative error $\bar{e}$) at optimal computational cost by choosing the appropriate number of Gauss points [71]. For the adaptive integral method, to avoid using excessively high Gauss orders m, the considered element is divided into sub-elements (with length L) to reduce the distance ratio. It should be pointed out that, for this method, the nearly singular integrals can be accurately evaluated by using normal Gauss orders due to the distance aspect ratio remaining stable and not too large. For the adaptive integral method, the following relations hold:

$$m=\sqrt{\frac{2}{3}\beta+\frac{2}{5}}\left[-\frac{1}{10}\ln\left(\frac{\bar{e}}{2}\right)\right]\left[\left(\frac{8L}{3d}\right)^{3/4}+1\right] \tag{17}$$

which can be rearranged to yield

$$L=\frac{3}{8}d\left(\frac{-10m}{\sqrt{2\beta/3+2/5}\ln(\bar{e}/2)}-1\right)^{4/3} \tag{18}$$

where β is the order of singularity for the integral and d represents the minimum distance from the computed point to the element. Therefore, by changing the values of upper bound of relative error $\bar{e}$ for the adaptive integral method, the computation accuracy of numerical integrals can be controlled. To avoid duplicate studies for adaptive integral methods, only some conclusions about adaptive integral methods are given in this work. For the interested reader, a study on the accuracy and number of optimal Gauss points about adaptive integral method can be found in Gong and Dong [71]. A detailed study on computational time has been given in Gong et al. [68,69].

Here, a simple curve element is considered, as shown in Fig. 1. The element is represented as a quadratic NURBS curve with knot vector $\Theta=\{0,0,0,1,1,1\}$, control points $P_1=(R\cos(\frac{\pi-2\theta}{4}),R\sin(\frac{\pi-2\theta}{4}))$, $P_2=(\frac{R}{\cos(\theta)}\cos(\frac{\pi}{4}),\frac{R}{\cos(\theta)}\sin(\frac{\pi}{4}))$, $P_3=(R\cos(\frac{\pi+2\theta}{4}),R\sin(\frac{\pi+2\theta}{4}))$ and weights $[1,\cos(\frac{\theta}{2}),1]$. In the computation, the radius R of the arc is fixed as 4.0 and $\theta=\pi/2$. The location of the source point is chosen as $\mathbf{y}=((R-d)\cos(\pi/4),(R-d)\sin(\pi/4))$, in which d is the distance from the source point to the curve element. We introduce the dimensionless aspect ratio $d^*=d/L$ to describe the proximity of the source point to the element, where L denotes the length of the element. In this study the distance d varies from 1 to 0.0000001. Since the computed point is close to the boundary, the integrals with kernel in Eqs. (7) and (8) will be nearly singular [65,68,69].

Fig. 2 (a) shows the relative error in evaluating the weak nearly singular integral by different methods (including Gauss–Legendre, adaptive integral method and exponential transformation method) as the computed point approaches the element.

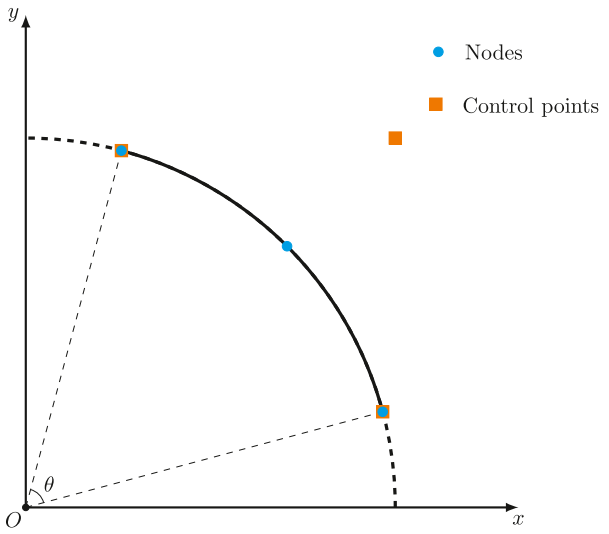

Fig. 1. The considered arc element.

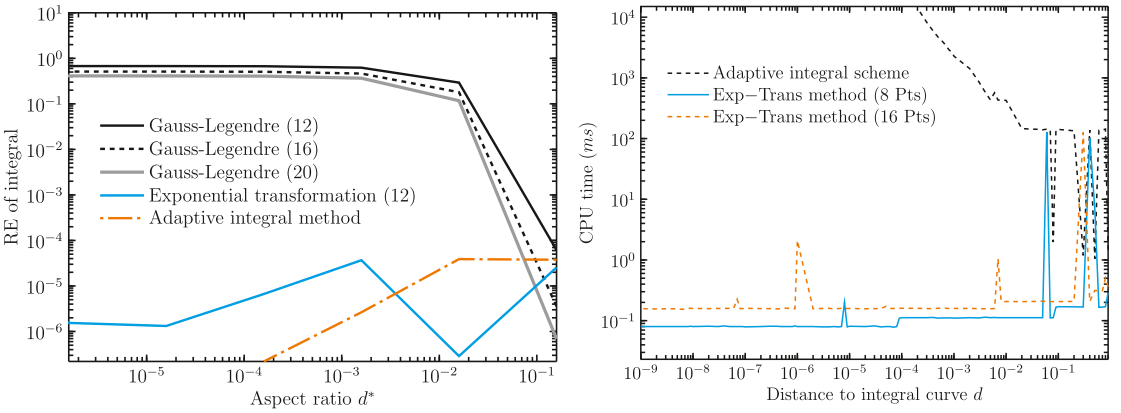

(a) Relative errors analysis (b) CPU time comparison

Fig. 2. Analysis of different methods for the evaluation of nearly singular boundary integrals.

For evaluations using the adaptive scheme, an upper bound relative error $\bar{e} = 10^{-10}$ is taken. By changing $\bar{e}$, we can achieve a desired accuracy for the computation of an integral. The relationships between $\bar{e}$, accuracy and efficiency for the adaptive integral scheme can be found in Gong et al. [68,69]. When the source point is not very close to the boundary, i.e. $d^* > 0.1$, all the considered methods (even the conventional Gauss–Legendre with 12 Gauss points) can be seen to yield accurate results. However, with the decrease of the aspect ratio d^*, the performance of Gaussian quadrature is less satisfactory. From Fig. 2(a), it can be seen that although the relative error obtained by conventional Gauss–Legendre shows a trend of convergence when the number of Gauss points increases from 12 to 20, the conventional Gauss–Legendre is unable to deliver a relative error below about 0.1 for the weak nearly singular integral. From Fig. 2(a), it is evident that the accuracy of exponential transformation and adaptive integral method remains quite satisfactory (less than 10^{-4}) down to $d^* < 10^{-6}$. The error analysis suggests that we can proceed focusing on the adaptive method and the exponential transformation method as the two preferred schemes.

As in the error analysis, we retain the use of $\bar{e} = 10^{-10}$ for the adaptive integral scheme. The CPU time for the adaptive integral scheme and exponential transformation (Exp-Trans) method is plotted in Fig. 2(b). The exponential transformation method CPU time is plotted for different Gauss points (8 and 16). And the required CPU time increases with the increase of the number of Gauss points used in the computation. The significant feature of the figure is that both the adaptive scheme and transformation method are efficient for aspect ratios $0.2 < d^* < 1$. However, for smaller d^* the transformation method will be the more efficient scheme. Therefore, we can introduce a critical aspect ratio d^*_{crit} to perform the hybrid integral scheme as given in Gong et al. [68,69]. Referring to Fig. 2, use of $d^*_{\text{crit}} = 10^{-3}$ looks to give accuracy with little cost. In the manuscript, we take the $d^*_{\text{crit}} = 10^{-3}$, unless otherwise stated.

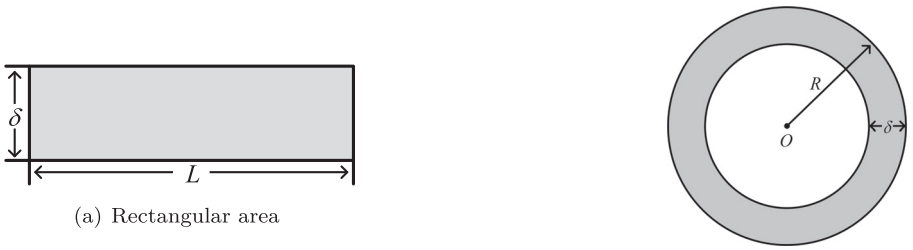

(a) Rectangular area

(b) Ring area

Fig. 3. Geometries of the considered heat sources.

In this section, we carry out an analysis on the errors and computational efficiency of Gauss–Legendre, exponential transformation and adaptive integral method for evaluating nearly singular integrals in a knot span. Through these results, we could draw a conclusion that using only one of the examined methods does not yield a satisfactory balance between accuracy and efficiency. But we can find that by using fixed number of Gauss point, the exponential transformation method performs well for small aspect ratio d^* and the adaptive scheme performs well for larger d^*. Therefore, it will be a good idea to inform a hybrid approach using the best features of exponential transformation method and adaptive integral scheme. The hybrid approach will introduce in Section 3. For the boundary element analysis, the integration is a major contributor to the overall run time of an analysis, and to alert the reader that a fuller presentation of CPU time for the whole analysis is to be given later.

2.5. Evaluation of domain integrals

The inclusion of a heat source $b(x)$ causes the integral equation in (6) to include a domain integral term, which at first sight appears to cause the BEM to lose one of its key advantages of involving only boundary integrals. In this section, the domain integral involved in Eq. (6) is transformed to a contour integral taken along the boundary of the heat source region and a radial integral by using the radial integration method [77].

Take the domain integral in Eq. (6) as an example. The domain integral is expressed as

$$I = \frac{1}{2\pi}\int_{\Omega} b(\mathbf{x}) \ln r(\mathbf{y},\mathbf{x}) d\Omega(\mathbf{x}) \tag{19}$$

in which $r(\mathbf{y},\mathbf{x})$ is the distance between the source point $\mathbf{y}$ to the field point $\mathbf{x} \in \Omega$.

In this work, a heat source with arbitrary geometry inside a substrate is considered. The heat source is active inside a region Ω_h with boundary Γ_h, embedded in the substrate Ω. If the source region Ω_h does not intersect the boundary, then the source point $\mathbf{y} \in \Gamma$ and field point $\mathbf{x} \in \Omega_h$ so $r(\mathbf{y},\mathbf{x}) \neq 0$ and the domain integrals are regular. By applying the radial integration method to integral (19), the domain integral can be transformed to a contour integral as follows,

$$I_\Omega = \frac{1}{2\pi}\int_{\Omega} b(\mathbf{x}) \ln r(\mathbf{y},\mathbf{x}) d\Omega(\mathbf{x}) = \frac{1}{2\pi}\int_{\Omega_h} b(\mathbf{x}) \ln r(\mathbf{y},\mathbf{x}) d\Omega_h(\mathbf{x}) = \frac{1}{2\pi}\int_{\Gamma_h} \frac{1}{r(\mathbf{y},\mathbf{x})}\frac{\partial r(\mathbf{y},\mathbf{x})}{\partial \mathbf{n}_h} F(\mathbf{y},\mathbf{x}) d\Gamma_h(\mathbf{x}) \tag{20}$$

where $\mathbf{n}_h$ is the unit outward normal vector to the boundary Γ_h, and

$$F(\mathbf{y},\mathbf{x}) = \int_0^{r(\mathbf{y},\mathbf{x})} rb(\mathbf{x}) \ln r(\mathbf{y},\mathbf{x}) dr \tag{21}$$

It is noted that the inclusion of term r in Eq. (21) cancels the logarithmic singularity and the integrals can be evaluated numerically using Gauss–Legendre quadrature. To test the effectiveness of the radial integration method for problems containing thin sections, the domain integral in Eq. (19) is evaluated over two different domains (including a $\delta \times L$ rectangular area and a ring area with $R = 2$ and thickness δ as shown in Fig. 3). It should be noted that the domains are described by NURBS, therefore no geometric errors will be incurred. Fig. 4(a) and (b) show the results of the domain integrals by the radial integration method for cases in which the thickness δ of the structure varies from 0.5 down to 10^{-8}. It is evident that the absolute value of integral I_Ω varies with δ in a way that demonstrates stability even for the smallest δ. In Fig. 4(a), the reason for the fluctuation of the curves is that the sign of the error changes at these points.

Following the method above, the domain integrals appearing in the boundary-domain integral equation (Eq. (6)) can be converted to contour integrals. Then, the following strictly boundary integral equation is formed,

$$c(\mathbf{y})u(\mathbf{y}) + \int_{\Gamma} Q(\mathbf{y},\mathbf{x})u(\mathbf{x}) d\Gamma(\mathbf{x}) = \int_{\Gamma} U(\mathbf{y},\mathbf{x})q(\mathbf{x}) d\Gamma(\mathbf{x}) - \frac{1}{2\pi}\int_{\Gamma_h} \frac{1}{r(\mathbf{y},\mathbf{x}')}\frac{\partial r(\mathbf{y},\mathbf{x}')}{\partial \mathbf{n}_h} F(\mathbf{y},\mathbf{x}') d\Gamma_h(\mathbf{x}') \tag{22}$$

In the current implementation of the IGABEM, the boundary Γ of considered substrate will be divided into 'elements', i.e. knot spans, Γ_e $(e = 1, 2, \ldots, N_e)$. In addition to evaluate the boundary integrals in the last term of Eq. (22), the boundary Γ_h of the heat source region is also subdivided, into N_e^h subdivisions, though it is noted that these subdivisions are for

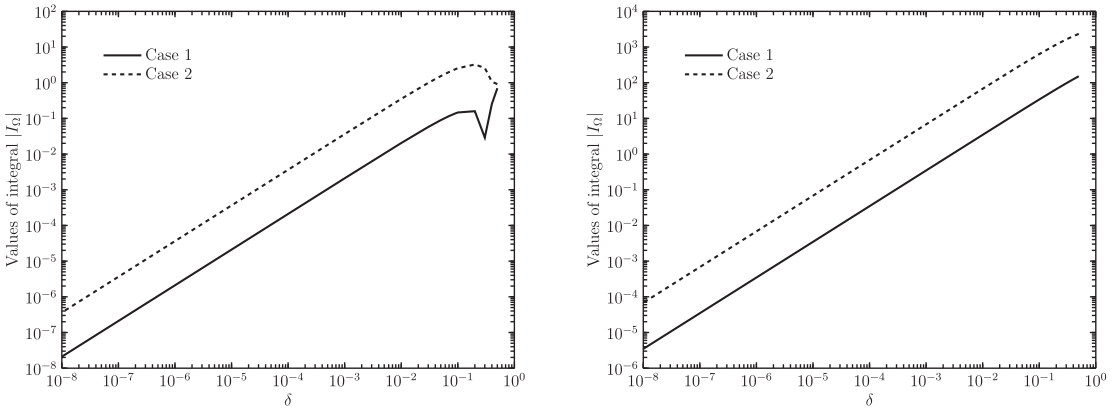

(a) $|I_\Omega|$ on rectangular area (b) $|I_\Omega|$ on ring area

Fig. 4. Values of integral $|I_\Omega|$ on different domains (case 1: $b(x) = 10^2$; Case 2: $10^3(x^2 + xy)$).

integration purposes only and do not contribute any degrees of freedom to the problem. Based on the NURBS expansion and geometry description in Section 2.3, the temperature and flux density in a knot span $[\xi_i, \xi_{i+1}]$ are expressed in a NURBS basis as

$$u(\xi) = \sum_{a=1}^{p+1} R_a(\xi)\tilde{u}_a, \tag{23}$$

$$q(\xi) = \sum_{a=1}^{p+1} R_a(\xi)\tilde{q}_a, \tag{24}$$

where $\tilde{u}_a$ and $\tilde{q}_a$ are the temperature and flux parameters, respectively, associated with the basis function with index a. Using these expansions of the temperature and flux density, the boundary integral equation in Eq. (22) can be written in a discretised form:

$$C(\zeta_c)\sum_{a_0=1}^{p+1} R_{e_0a_0}(\zeta_c)\tilde{u}_{e_0a_0} + \sum_{e=1}^{N_e}\sum_{a=1}^{p+1} \mathrm{Q}_{ea}\left(\zeta_c, \hat{\xi}_e\right)\tilde{u}_{ea} = \sum_{e=1}^{N_e}\sum_{a=1}^{p+1} \mathrm{U}_{ea}\left(\zeta_c, \hat{\xi}_e\right)\tilde{q}_{ea} + \sum_{e=1}^{N_e^h}\sum_{a=1}^{p+1} \mathrm{D}_{ea}\left(\zeta_c, \hat{\xi}_e\right) \tag{25}$$

where c is the collocation point index; ζ_c represents the knot vector coordinate of the collocation point; e denotes the element index; symbols having an index with a subscript '0' (i.e. a_0, e_0) indicate that the element is that on which the collocation point is located. $\hat{\xi}_e \in [-1, 1]$ is the local coordinate of the field point in the eth knot span. a is the local index of a basis function (or control point) in the eth element. Boundary integrals Q_{ea}, U_{ea} and U_{ea} are expressed as

$$\mathrm{Q}_{ea}(\zeta_c, \hat{\xi}_e) = \int_{-1}^{1} \mathrm{Q}(\zeta_c, \hat{\xi}_e) R_{ea}(\hat{\xi}_e) J_e(\hat{\xi}_e) d\hat{\xi}_e \tag{26}$$

$$\mathrm{U}_{ea}(\zeta_c, \hat{\xi}_e) = \int_{-1}^{1} U(\zeta_c, \hat{\xi}_e) R_{ea}(\hat{\xi}_e) J_e(\hat{\xi}_e) d\hat{\xi}_e \tag{27}$$

$$\mathrm{D}_{ea}(\zeta_c, \hat{\xi}_e) = -\frac{1}{2\pi}\int_{-1}^{1} \frac{1}{r(\zeta_c, \hat{\xi}_e)} \frac{\partial r(\zeta_c, \hat{\xi}_e)}{\partial \mathbf{n}_h} F(\zeta_c, \hat{\xi}_e) J_e(\hat{\xi}_e) d\hat{\xi}_e \tag{28}$$

in which R_{ea} is the ath basis function in the eth knot span. The Jacobian $J_e(\hat{\xi}_e)$ may be computed using

$$J_e(\hat{\xi}_e) = \frac{d\Gamma}{d\hat{\xi}_e} = \frac{d\Gamma}{d\xi}\frac{d\xi}{d\hat{\xi}_e} \tag{29}$$

3. Treatment of integrals in IGABEM for multi-scale structures

One of the appealing features of IGABEM is that the accurate geometric description can often mean that larger elements can be permitted than in conventional polynomial BEM formulations. In order to exploit this feature to enhance computational efficiency for multiscale problems, it is important to develop bespoke integration schemes that provide accurate evaluations of the large number of integrals in IGABEM including regular, weakly singular, strongly singular and nearly singular

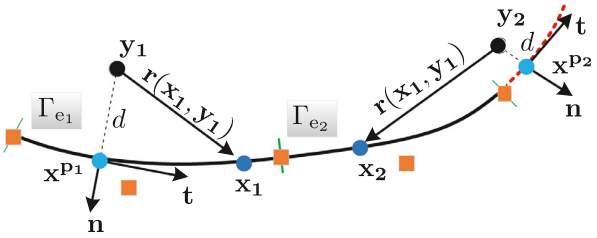

Fig. 5. Minimum distance d to the element for cases when $\mathbf{x}^{\mathbf{p_1}} \in \mathbf{\Gamma}_{\mathbf{e_1}}$ and $\mathbf{x}^{\mathbf{p_2}} \notin \mathbf{\Gamma}_{\mathbf{e_2}}$. Dashed red line is the analytical extension of Γ_{e_2}.

cases. Although a multiscale geometry can be described by a small number of boundary elements, the areas of adjacent isogeometric boundary elements may become very different, and this presents challenges in evaluating the nearly singular integrals over the larger element when the collocation point lies within the smaller element. If a standard quadrature scheme such as Gauss–Legendre is employed, a very high order Gauss scheme is needed; the kernel functions will be evaluated many millions of times and the computational cost will quickly become prohibitive. In [71], the adaptive integration method presented by Gao and Davies [70] is extended to IGABEM, which delivers high accuracy at minimum computational cost for boundary integrals on an isogeometric element. The adaptive integral scheme will be adopted to compute the regular integrals over an isogeometric element for multiscale geometry structures.

Several integration methods originally developed for conventional BEM are being adapted to deal with the singular integrals in IGABEM. For example, Simpson et al. [49] used the subtraction of singularity method and Telles transformation to evaluate strongly and weakly singular integrals, respectively. In [79] the power series expansion method is used to evaluate the strongly and weakly singular integrals in 3D IGABEM. The nearly singular integrals in IGABEM can be computed by a semianalytical analysis method [67], adaptive integration method [80], or transformation method [65]. Recently, Gong et al. [68,69] developed a hybrid integration scheme for the nearly singular integrals in the 2D/3D IGABEM. The method is capable of producing accurate and efficient solutions for challenging geometries. In this work, the hybrid integration scheme is used to evaluate the nearly singular integrals arising in the IGABEM for multiscale geometry problems.

3.1. Hybrid integration scheme for multiscale geometry structures

In this work, we focus our attention on the analysis of heat transfer problems in multiscale geometry problems. Thus, only some conclusions about the hybrid integration method are given; more details about the scheme can be found in Gong et al. [68,69].

Each integral considers a pairing of source point and an isogeometric element Γ_e with knot span $[\xi_i, \xi_{i+1}]$. The challenging nearly singular integrals arise when the source point is very close to, but does not lie on, the element. To describe the proximity of the source point to an isogeometric boundary element, we define an aspect ratio $d^* = d/L$, where L is the length of the element and d denotes the minimum distance from the source point to the element. For cases in which the aspect ratio d^* is larger than a given critical value d^*_{crit}, the integral is considered sufficiently regular that the adaptive integration scheme can be efficiently applied. However, if the aspect ratio $d^* < d^*_{\text{crit}}$, this corresponds to a very nearly singular integral and an exponential transformation method is used.

For an isogeometric element Γ_{e_1} shown in Fig. 5, when the projection point $\mathbf{x}^{p_1} \in \Gamma_{e_1}$ the minimum distance d from the source point $\mathbf{y}_1$ to the integration element is defined as perpendicular to the tangential line, through the projection point $\mathbf{x}^{p_1}(\xi_{p_1})$ and source point $\mathbf{y}_1(\xi)$. It should be pointed out that for some cases the projection point might be outside the element, i.e. $\mathbf{x}^{\mathbf{p_2}} \notin \mathbf{\Gamma}_{\mathbf{e_2}}$, as shown in Fig. 5. Since the NURBS basis functions are a set of continuous functions of knot ξ, we can apply them to values of parameter ξ outside the knot span of the element [68,69]. And the dashed red line in Fig. 5 shows the analytical extension of Γ_{e_2}. For this case, the minimum distance d can still be computed by $d = |\mathbf{y}_2(\xi) - \mathbf{x}^{\mathbf{p_2}}|$.

We start by writing a Taylor expansion of the field point location $\mathbf{x}$ in the neighborhood of the projection point $\mathbf{x}^p$,

$$x_k - y_k = dn_k(\xi_p) + D^1_{k,\xi}(\xi - \xi_p) + D^2_{k,\xi}(\xi - \xi_p)^2 + \ldots + D^n_{k,\xi}(\xi - \xi_p)^n + \text{HOT} \tag{30}$$

where $k = 1, 2$, $\mathbf{x} = (x_1, x_2)$, $\mathbf{y} = (y_1, y_2)$, n represents the order of the Taylor expansion, HOT abbreviates Higher Order Terms and the coefficients D are defined as

$$D^n_{k,\xi} = \frac{1}{n!}\frac{d^n x_k}{d\xi^n}\bigg|_{\xi=\xi_p} \tag{31}$$

Since the normal $\mathbf{n}(n_1, n_2)$ and tangential direction $(\frac{dx_1}{d\xi}, \frac{dx_2}{d\xi})$ are two mutually perpendicular lines, the term $n_k D^1_{k,\xi} = 0$. Then, the square of the distance from the source point to the field point, i.e. r^2, can be expressed as

$$r^2(\xi) = d^2 + (\xi - \xi_p)^2 g_n(\xi) + E_{\text{trun}} \tag{32}$$

where $\xi \in [\xi_i, \xi_{i+1}]$, g_n contains the sums of products of terms in the Taylor expansion and E_{trun} is the truncation error caused by neglecting the HOT in Eq. (30).

Then, an exponential transformation method which has been used to deal with the nearly singular integrals in conventional BEM [81–83] will be adopted in this work. A nonlinear coordinate transformation mapping from $\mu \in [-1, 1]$ to the parametric coordinate $\xi \in [\xi_i, \xi_{i+1}]$ is defined as

$$\xi = d\left(e^{k(1+\mu)}\right) + \xi_p \tag{33}$$

where

$$k = 0.5 \ln\left(1 + \frac{A}{d}\right). \tag{34}$$

Here, the symbol A, related to knots ξ_i, ξ_{i+1} $(i = 1, 2, \ldots)$ and parameter ξ_p, can be expressed as

$$A = \begin{cases} \xi_p - \xi_i, & \text{if } \xi_p > \xi_i, \\ \xi_{i+1} - \xi_p, & \text{if } \xi_p < \xi_{i+1}. \end{cases} \tag{35}$$

The Jacobian of this transformation can be described by

$$J = \frac{d\xi}{d\mu} = k \cdot d \cdot e^{k(1+\mu)}. \tag{36}$$

Substituting Eq. (33) into (32), we obtain

$$r^2(\xi) = d^2\left[1 + (e^{k(1+\mu)})^2 g_n(\xi)\right] + E_{\text{trun}} \tag{37}$$

Substituting the above distance function into the boundary integrals with fundamental solutions, we can obtain the following equations

$$I_1 = \int_{\xi_i}^{\xi_{i+1}} f(\xi) \ln r^2 d\xi = \int_{\xi_i}^{\xi_{i+1}} f(\xi) \ln\left(d^2\left[1+(e^{k(1+\mu)})^2 g_n(\xi)\right] + E_{\text{trun}}\right) k \cdot d \cdot e^{k(1+\mu)} d\xi \tag{38}$$

$$I_2 = \int_{\xi_i}^{\xi_{i+1}} \frac{f(\xi)}{r^2} d\xi = \int_{\xi_i}^{\xi_{i+1}} \frac{f(\xi) k \cdot d \cdot e^{k(1+\mu)}}{d^2\left[1+(e^{k(1+\mu)})^2 g_n(\xi)\right] + E_{\text{trun}}} d\xi \tag{39}$$

Since the term d^2 in the above equation is constant, and neglecting the error term E_{trun}, the term d^2 can be moved out of the boundary integrals. Then, the near singularity of the boundary integrals will be fully regularized and the integrals can be evaluated using standard Gaussian quadrature.

In the computation of these integrals, some errors caused by neglecting the truncation term E_{trun} are introduced. In [68,69], the relationships between the accuracy and truncation error of the Taylor expansion for an isogeometric boundary element are discussed. The conclusion drawn from that work is that the truncation errors grow with the increasing of the distance between the field point and the projection point. Here, only some conclusions are used; more details can be found in Gong et al. [68,69].

Since the range of sizes of isogeometric boundary elements can be very large in modeling multiscale structures, a hybrid integral scheme which combines the exponential transformation method and adaptive integral method is developed. In the evaluation of an integral over an isogeometric boundary element with knot span $[\xi_i, \xi_{i+1}]$, we will first compute the element ratio $d^*(= d/L)$. If the value of $d^* > d^*_{\text{crit}}$, the integral will be a regular integral and computed by adaptive integral method (note that the critical aspect ratio d^*_{crit} has not yet been specified; it will be determined through numerical testing). These boundary element integrations (including some weakly near-singular integrals) can be computed easily and effectively at optimal computational cost by choosing an optimal order of Gauss integration order. However, with the increase of the near-singularity ($d^* < d^*_{\text{crit}}$), the CPU time by using the adaptive integral method will increase sharply (as shown in Fig. 2(b)). Therefore, the proposed hybrid integral scheme in this work will be applied.

For an integral evaluated by the hybrid integral scheme, the truncation error E_{trun} in Eqs. (37)–(39) will be neglected. The truncation error E_{trun} can be computed using

$$\text{Relative error } (\text{RE}_{\text{Taylor}}) = \left| \frac{r^2_{\text{exact}} - \left(d^2[1 + (e^{k(1+\mu)})^2 g_n(\xi)]\right)}{r^2_{\text{exact}}} \right| \tag{40}$$

where r^2_{exact} is the exact square distance between the source point (y_1, y_2) and Gauss point (x_1, x_2). It should be noted that both the coordinates of source point and field point at the location of the Gauss point are known in the computation. The truncation error $(\text{RE}_{\text{Taylor}})$ will grow with increasing distance between the field point and the projection point, as discussed in Gong et al. [68]. In the computation of the nearly singular integral, if values of $\text{RE}_{\text{Taylor}}$ exceed a specified tolerance *eps* at the location of Gauss point $\xi = \xi'_1$ and $\xi = \xi'_2$, the integral will be subdivided into three parts over parametric domains $[\xi_1, \xi'_1]$, $[\xi'_1, \xi'_2]$ and $[\xi'_2, \xi_2]$. For example, the integral in (39) can be expressed as

$$\int_{\xi_1}^{\xi_2} \frac{f(\xi)}{r^2} d\xi = \int_{\xi_1}^{\xi'_1} \frac{f(\xi)}{r^2} d\xi + \int_{\xi'_1}^{\xi'_2} \frac{f(\xi)}{r^2} d\xi + \int_{\xi'_2}^{\xi_2} \frac{f(\xi)}{r^2} d\xi \tag{41}$$

Table 1
Expressions of resulted integrals by hybrid integration scheme (f represents the entire integrand; assume projection point $\xi_p \in [\xi_1, \xi_2]$).

Cases	Relationship of parameters	Resulted sub-regions	Integral I_e
Case 1	$\xi_1 \le \xi_1' \le \xi_2' \le \xi_2$	$[\xi_1, \xi_1'], [\xi_1', \xi_2'], [\xi_2', \xi_2]$	$= \int_{\xi_1}^{\xi_1'} f d\xi + \int_{\xi_1'}^{\xi_2'} f d\xi + \int_{\xi_2'}^{\xi_2} f d\xi$
Case 2	$\xi_1' \le \xi_1 \le \xi_2' \le \xi_2$	$[\xi_1, \xi_2], [\xi_2', \xi_2]$	$= \int_{\xi_1}^{\xi_2'} f d\xi + \int_{\xi_2'}^{\xi_2} f d\xi$
Case 3	$\xi_1 \le \xi_1' \le \xi_2 \le \xi_2'$	$[\xi_1, \xi_1'], [\xi_1', \xi_2]$	$= \int_{\xi_1}^{\xi_1'} f d\xi + \int_{\xi_1'}^{\xi_2} f d\xi$
Case 4	$\xi_1' \le \xi_1 \le \xi_2 \le \xi_2'$	$[\xi_1, \xi_2]$	$= \int_{\xi_1}^{\xi_2} f d\xi$

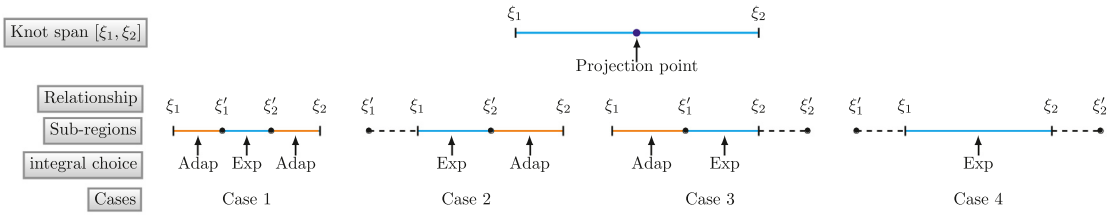

Fig. 6. Integral method in hybrid integration scheme. "Exp" and "Adap" represent exponential transformation method and adaptive integration scheme, respectively.

In the hybrid integral scheme, if $\mathrm{RE}_{\mathrm{Taylor}} > eps$ in domains $[\xi_1, \xi_1']$ and $[\xi_2', \xi_2]$, the adaptive integration scheme will be used in the two sub-regions. The exponential transformation method will be applied in the central region $[\xi_1', \xi_2']$ to improve the computational efficiency by using a fixed quadrature order. Some care is needed in order for the scheme to be robust in dealing with various different relationships between ξ_1, ξ_1', ξ_2 and ξ_2'. Since $\mathrm{RE}_{\mathrm{Taylor}} < eps$ in domain $[\xi_1', \xi_2']$ for cases 1–4 in Table 1, the exponential transformation method will be used in the integrals over these domains. The choice of integral method for the four cases is given in Fig. 6.

The overall integration strategy for the current IGABEM is summarized in Fig. 7.

4. Implementation of current isogeometric boundary element method

By using the special integration schemes in Fig. 7, the integrals in Eqs. (26)––(28) can be evaluated. By considering Eq. (25) at all the n collocation points (equal to the number of control points, or NURBS basis functions) located at the Greville abscissae, a linear system of equations can be obtained:

$$\mathbf{H}\tilde{\mathbf{u}} = \mathbf{G}\tilde{\mathbf{t}} + \mathbf{y} \tag{42}$$

where matrix $\mathbf{H}$ contains jump terms and integrals in (26). Since temperature u is a continuous scalar, there is only one unknown temperature coefficient for each degree of freedom and $\mathbf{H}$ becomes a square matrix. However, the normal flux density q is discontinuous at corners and, in the same fashion as conventional BEM formulations, $\mathbf{G}$ becomes a rectangular matrix containing boundary integrals in (27). Vectors $\tilde{\mathbf{u}}$ and $\tilde{\mathbf{t}}$ contain the corresponding temperature and flux coefficients that multiply the NURBS basis functions, respectively. The vector $\mathbf{y}$ is produced by the domain integral in Eq. (6).

Applying boundary conditions and rearranging Eq. (42) in the standard BEM fashion, the following linear system can be assembled:

$$\mathbf{A}\lambda = \mathbf{b} \tag{43}$$

where matrix $\mathbf{A}$ contains the appropriate columns of matrices $\mathbf{G}$ and $\mathbf{H}$ that multiply the unknown degrees of freedom. Vector λ contains the unknown temperature and flux coefficients corresponding to the NURBS basis functions. The (known) right hand side vector $\mathbf{b}$ contains not only the vector $\mathbf{y}$ but also the products of the terms in $\tilde{\mathbf{u}}$ and $\tilde{\mathbf{t}}$ that are prescribed boundary conditions and the corresponding columns of $\mathbf{H}$ and $\mathbf{G}$. By solving the linear system in (43), all the unknown coefficients of temperature and heat flux can be obtained. The temperature and flux density distributions around the boundary can then be recovered from (23) and (24).

As a postprocessing step, the temperature at any interior point P can be simply computed by the BIE for interior point in Eq. (44).

$$u(P) = -\int_{\Gamma} U(P, \mathbf{x}) q(\mathbf{x}) d\Gamma(\mathbf{x}) + \int_{\Gamma} Q(P, \mathbf{x}) t(\mathbf{x}) d\Gamma(\mathbf{x}) - \frac{1}{2\pi} \int_{\Gamma_h} \frac{1}{r(P, \mathbf{x}')} \frac{\partial r(P, \mathbf{x}')}{\partial \mathbf{n}_h} F(P, \mathbf{x}') d\Gamma_h(\mathbf{x}') \tag{44}$$

5. Numerical results and discussion

In this section, several numerical examples are presented to demonstrate the performance of the IGABEM. Unless otherwise stated, we take the critical aspect ratio $d^*_{\mathrm{crit}} = 10^{-3}$ and tolerance $eps = 10^{-6}$. In this section, we choose some simple

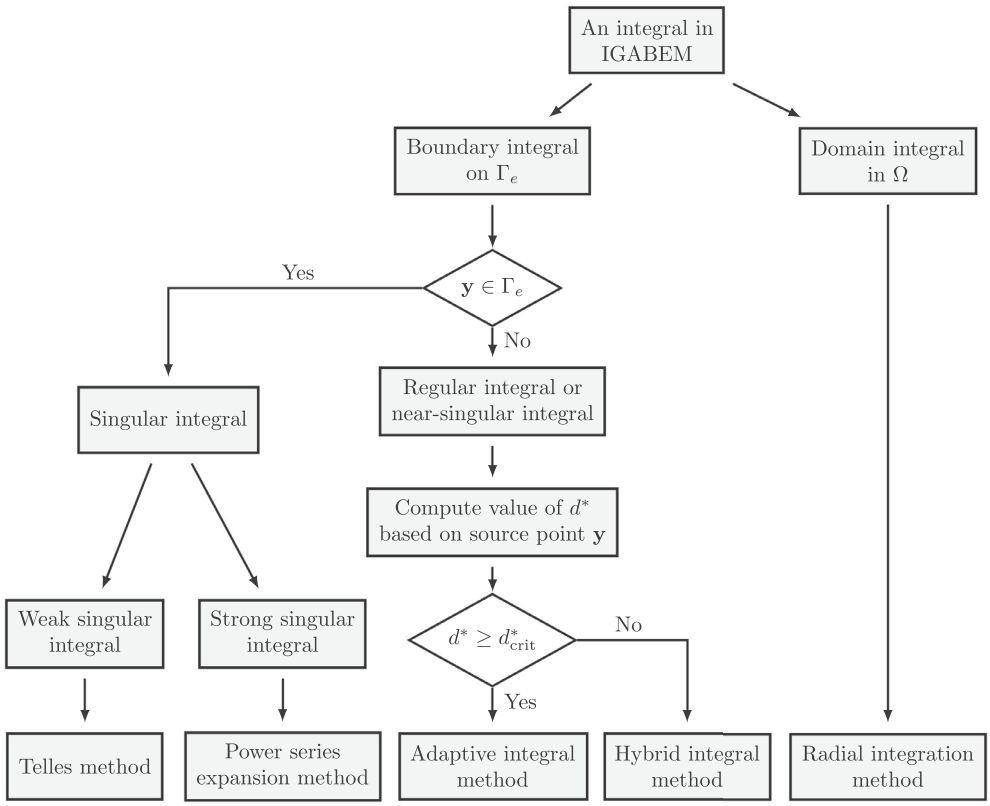

Fig. 7. Choice of integral method.

solution fields in order to be able to compute errors precisely and demonstrate the convergence of the method. A propeller model (with complex boundary geometry) is used to demonstrate the benefits of the proposed IGABEM scheme. Then, a single heat source model (the flower-shaped source) is added. The flower-shaped source can make use of the exact geometric definition of the source. Later, a model with circular arc features on the exterior boundary is considered. Finally, some models with multiscale features are analyzed by the current scheme. We also introduce a model of a real physical problem and replace the Dirichlet boundaries around the cooling fins with convective boundaries.

For the boundary element method, the numerical accuracy of unknown boundary quantities is one of the key metrics. To a large extent, the numerical accuracy of boundary quantities determines the numerical accuracy of interior quantities. This is because, once the boundary flux $q(x)$ and temperature $u(x)$ are known, the temperature can be computed at any point P in the domain Ω by evaluating the integrals in the boundary integral equation (Eq. (44)). All terms inside the integrals are known, so $u(P)$ can be easily found. For this reason, BEM researchers usually show the L^2 relative error norm of the boundary quantities.

To carry out the accuracy and convergence analysis, several types of errors are considered: a relative error defined in Eq. (40) and the L^2 relative error norm with respect to a reference solution f_{exact} defined by

$$E_2(f_{\text{num}}; \Gamma) = \frac{\|f_{\text{num}} - f_{\text{exact}}\|_{L^2(\Gamma)}}{\|f_{\text{exact}}\|_{L^2(\Gamma)}} \tag{45}$$

where Γ is the boundary of the propeller, f_{num} is the boundary quantities (temperature or heat flux) as predicted by the present numerical scheme, and the L^2 norm is

$$\|f\|_{L^2(\Gamma)} = \sqrt{\int_\Gamma F^2 d\Gamma}$$

To show the proposed scheme's accuracy on overall domain, a relative error norm taken by integration over a domain is defined, i.e. a single number produced by the calculation:

$$E_2(T_{\text{num}}; \Omega) = \frac{\|T_{\text{num}} - T_{\text{exact}}\|_{L^2(\Omega)}}{\|T_{\text{exact}}\|_{L^2(\Omega)}} \tag{46}$$

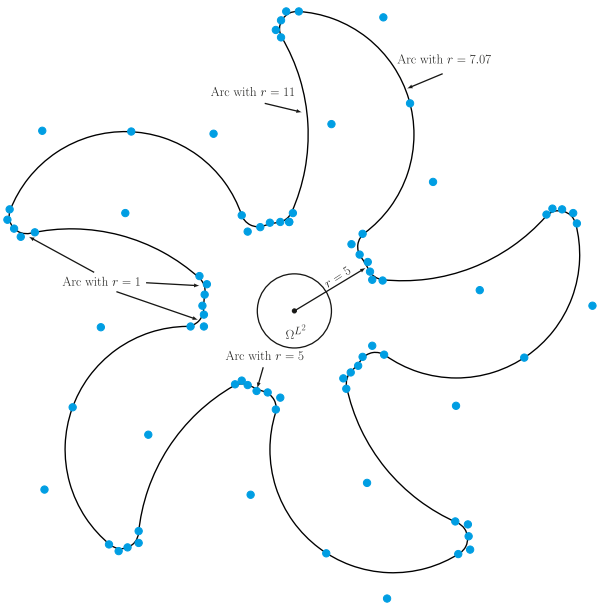

Fig. 8. Geometry description for propeller model.

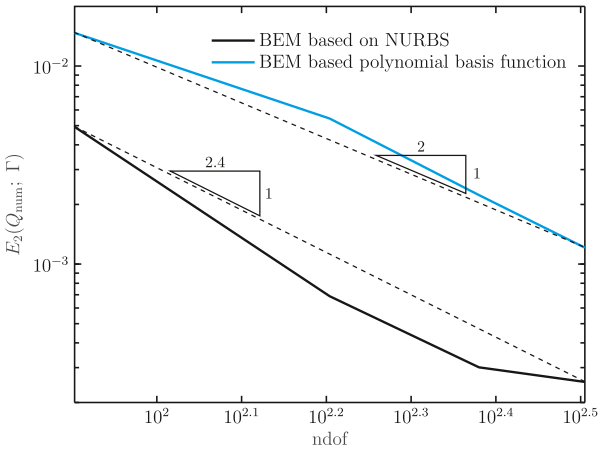

Fig. 9. L^2 relative error norm $E_2(Q_{\text{num};\Gamma})$ for different methods.

where Ω is a domain inside the propeller, T_{num} is the temperature obtained by the present numerical scheme, and the L^2 norm over a domain is

$$\|f\|_{L^2(\Omega)} = \sqrt{\int_\Omega f^2 d\Omega}$$

Unless otherwise stated, we take the degree of the NURBS basis functions $p = 2$ for all examples. For the conventional BEM, both the geometries and physical quantities are described by quadratic polynomial shape functions.

5.1. Propeller model

To verify the ability of the proposed method to handle complex engineering geometries, a propeller is analyzed with the temperature boundary condition $T(x, y) = 10x + 8y$. As shown in Fig. 8, the inner and outer radius of the blade are taken as $r_1 = 11$ and $r_2 = 7.0711$, respectively. the radius of inner circle is $r_3 = 5$. Some small arc curves with $r_4 = r_5 = 1$ are used to replace sharp corners in the model.

For this problem, the analytical solution of boundary heat flux is $Q_{\text{exact}} = 10n_1 + 8n_2$, n_i $(i = 1, 2)$ is the ith component of the unit outward normal vector.

In Fig. 9, we present the L^2 relative error norm $E_2(Q_{\text{num}};\Gamma)$ when different schemes are used. It is evident that both the BEM based on NURBS and conventional polynomial basis can obtain accurate results. But the $E_2(Q_{\text{num}};\Gamma)$ obtained by

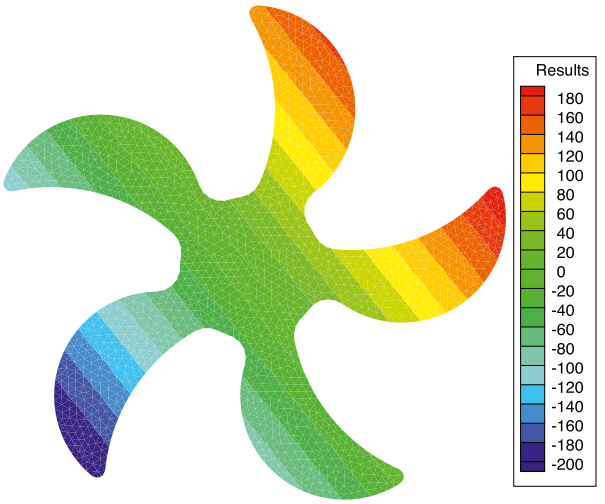

Fig. 10. Results distribution obtained with ndof = 160.

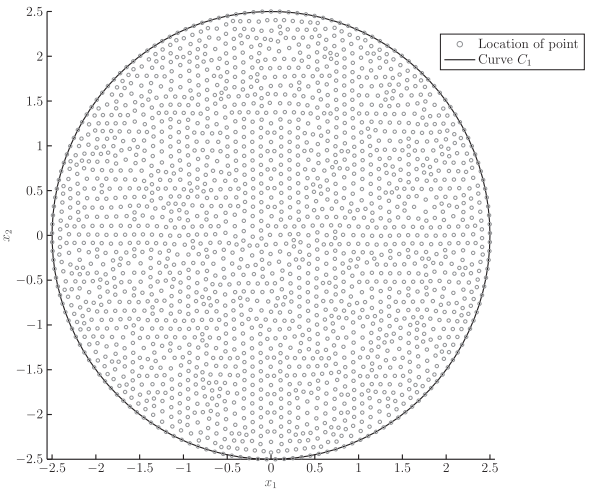

Fig. 11. Locations of computed points inside the domain.

BEM based on NURBS (i.e. IGABEM) is smaller than that obtained by BEM based on the polynomial shape functions when ndof is the same. IGABEM gives improved results because of the exact geometric definition, yes, but also because the basis functions are smoother and non-negative. As is shown in Fig. 9 that, even when ndof is large (and the elements become so small that the geometric error is small) IGABEM is still better because of the second reason. Finally, using ndof = 160, the temperature distribution inside the model is given in Fig. 10. For the computation, the L^2 relative error norm $E_2(Q_{\text{num}}; \Gamma)$ is 6.884×10^{-4}.

5.2. Rectangular area with heat sources

Here, a 10×10 rectangular silicon die with different heat sources is investigated. The thermal conductivity of the silicon die is taken as $K_h = 148$ W/(m K) [84]. The temperatures on the left and right sides are 20°C and 80°C, respectively. The upper and lower boundaries are insulated, i.e. $\Delta T \cdot \mathbf{n} = 0$. The initial parametric definition of the silicon die is given by a knot vector $\Theta = \{0, 0, 0, 1, 1, 2, 2, 3, 3, 4, 4, 4\}$. The boundary geometry of the silicon die is described by NURBS basis functions with order $p = 2$. In this example, three different inner heat sources are selected, Case 1: $b(x) = 100$ W/m^2; Case 2: $b(x) = 2500 \sin(e^{x+y})$ W/m^2; Case 3: $b(x) = 1000(x^2 + xy)$ W/m^2. Firstly, a circular heat source with radius $R = 2.5$ inside the silicon die is considered. To illustrate the accuracy of the current scheme, a set of internal points (shown in Fig. 11) is distributed along and inside curve C_1 (part of the boundary of the heat source) with definition

$$C_1 = \{(x, y) : x = R\cos\theta, y = R\sin\theta, \theta \in [0, \pi], R = 2.5\} \tag{47}$$

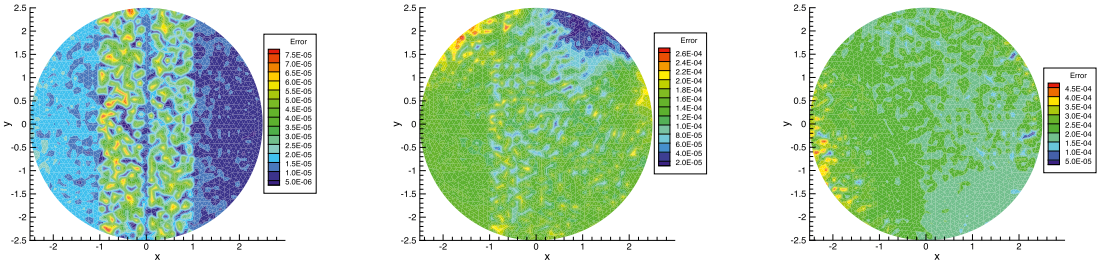

(a) $b(x) = 100$ (b) $b(x) = 2500\sin(e^{x+y})$ (c) $b(x) = 1000(x^2 + xy)$

Fig. 12. Temperature differences (errors defined in Eq. (40)) of results obtained by current scheme and finite element method.

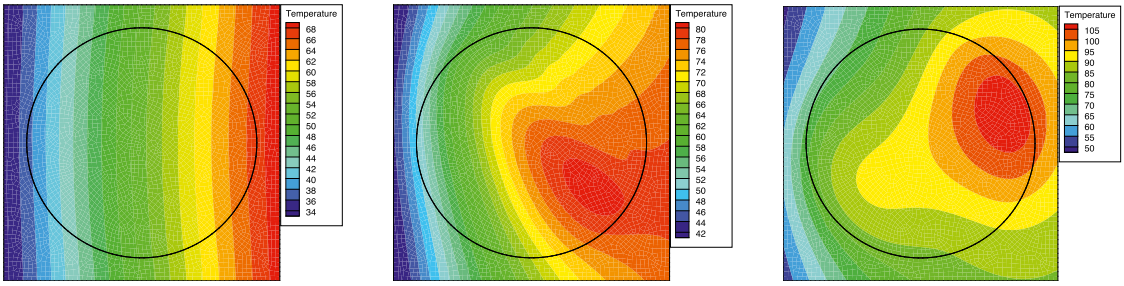

(a) $b(x) = 100$ (b) $b(x) = 2500\sin(e^{x+y})$ (c) $b(x) = 1000(x^2 + xy)$

Fig. 13. Temperature distribution inside the silicon die for the circular heat source.

Fig. 12 (a)–(c) show us the differences (or errors) of results obtained by current method (with ndof = 80) and finite element method. To offer reference solutions, the finite element models are constructed with the FEM software Abaqus. Triangle elements are employed, where the edge length of the elements in the model is 0.1. A refined mesh consisting of 20626 elements and 10514 nodes is used in the FEM model. In these figures, temperatures at same points (given in Fig. 11) are evaluated by using the two methods, respectively. Then the relative errors defined by Eq. (48) are computed and given in Fig. 12.

$$\mathrm{RE} = \frac{|f_{\mathrm{num}} - f_{\mathrm{ref}}|}{|f_{\mathrm{ref}}|} \tag{48}$$

where f_{num} denotes the values (temperature, in this case) computed by the current numerical method and f_{ref} denotes the values obtained from the reference solution. From these figures, we can find that the differences of solutions obtained by current scheme and Abaqus are very small. When the heat source $b(x)$ changes from 100 to $2500\sin(e^{x+y})$ or $1000(x^2 + xy)$, the differences will increase one order of magnitude. But the current scheme remains capable of delivering high accuracy of results with errors $< 10^{-4}$ even for complex heat source.

Fig. 13 (a)–(c) show the temperature distributions obtained by the present scheme corresponding to the three cases. From these figures, we can find that the temperature results in Fig. 13(b) and (c) are quite oscillatory which is a real effect caused by the particular source term.

Next we consider a heat source with complex geometries as shown in Fig. 14. Here, the temperatures of the rectangular silicon die on the left and right sides remain 20°C and 80°C. The flower-shaped heat source (which can demonstrate the benefits of IGABEM) will be used to replace the circular source. To show the numerical error of the current scheme inside the domain, a set of 1651 internal points (shown in Fig. 15) is distributed inside the heat source.

We will begin our heat transfer analysis and the inner heat source will be selected as $b(x) = 1000(x^2 + xy)$ W/m^2. In this heat source model shown in Fig. 14 and for which the temperature distribution obtained by the current method is shown in Fig. 16. Fig. 17 shows us the differences (errors) of results at 1651 internal points (shown in Fig. 15) obtained by current method (with ndof = 24) and finite element method. Since we can not obtain the analytical solutions, finite element models with refined meshes are still constructed by using the commercial software. From Fig. 17 we can find that the current scheme can obtain very accurate results even when the ndof = 24.

Fig. 18 shows the relative errors, RE, in temperature along the curve C_2 (shown in Figs. 14 and 15) as the number of degrees of freedom (ndof) increases from 8 to 24. The relative errors are taken with respect to a reference solution derived from very refined Abaqus FEM model, containing 12,191 elements and 11,696 nodes.From Fig. 18, we can see the proposed

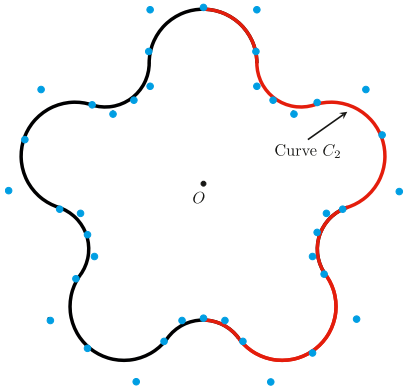

Fig. 14. The isogeometric model of a flower-shaped heat source.

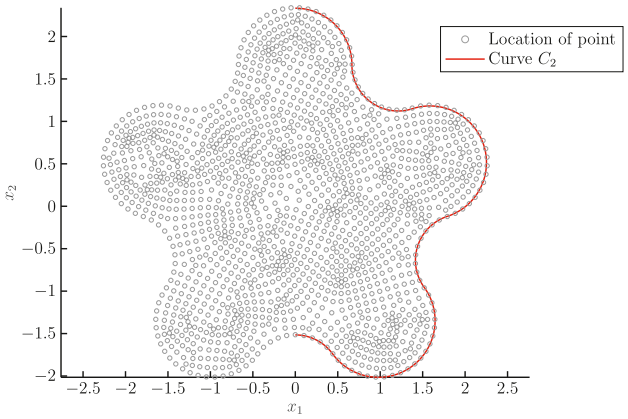

Fig. 15. Locations of computed points inside the domain.

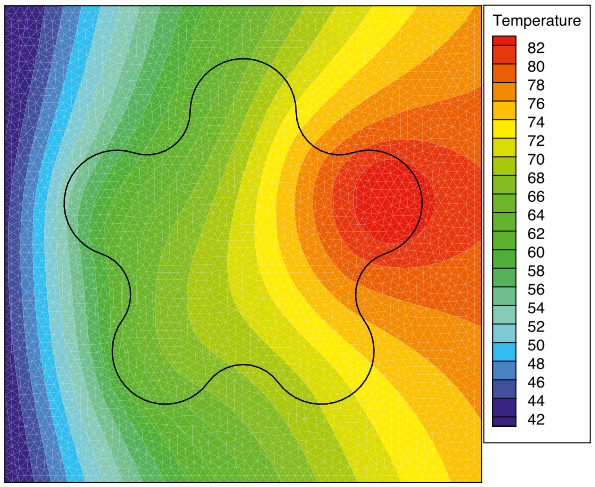

Fig. 16. Temperature distribution inside the matrix for the complex heat source.

scheme is able to deliver accurate results for this model even for a very small model with number of degrees of freedom, ndof = 8. A significant improvement in accuracy can be seen when the model is refined to ndof = 16, 24. It should be remembered that there are *no degrees of freedom* associated with the boundary of the source; only boundary degrees of freedom are required.

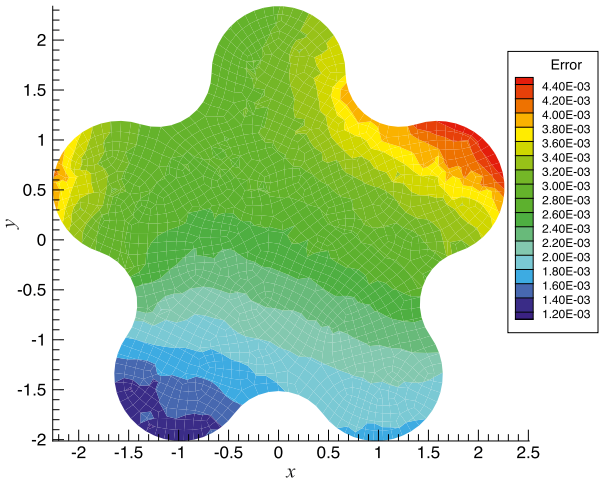

Fig. 17. Differences of temperature obtained by current scheme and finite element method when ndof = 24.

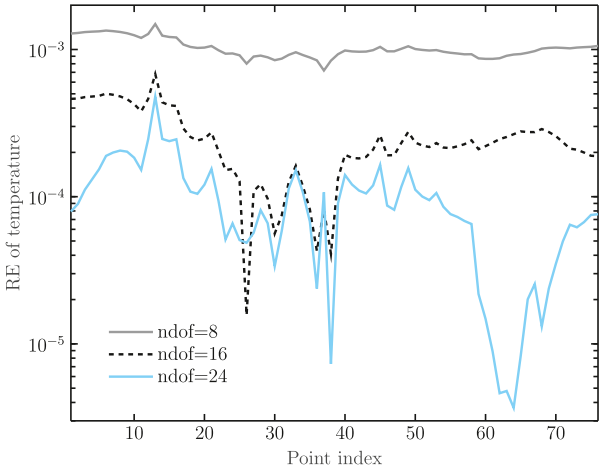

Fig. 18. Relative error of temperature along curve C_2 for different ndofs.

5.3. Rectangular area with arbitrary heat sources—heat lines

Similar to the above example, a highly convoluted heat pipe (shown in Fig. 19) is embedded in a 10×10 rectangular substrate. Here, the temperatures on the left and right sides of the substrate are prescribed as boundary conditions, being 20 °C and 80 °C, respectively. The heat source is expressed as $b(x) = 2500\sin(e^{x+y})$ W/m^2. The control points and other geometric parameters are also shown in that figure. Fig. 20 presents the relative error of temperature along the line C_3 (displayed in red in Fig. 19), for different model sizes. The line C_3 is defined as

$$C_3 = \{(x, y) : x = 2.0, y \in [-3.7, 3.7]\} \tag{49}$$

The reference solutions are obtained from a very refined FEM model consisting of 86,090 elements and 43,446 nodes.

From Fig. 20, it can be seen that when ndof = 8, the obtained results are unsatisfactory, demonstrating that the temperature field cannot be resolved successfully with such a coarse discretisation when the heat source has such a complex geometry. As the number of degrees of freedom (ndof) increases from 8 to 48, the convergence can be seen clearly, with highly accurate solutions ($10^{-6} < \mathrm{RE} < 10^{-4}$) achieved for ndof = 48. Fig. 21 shows the temperature contours through the model for the quadratic heat source.

5.4. Heat transfer for multiscale models with heat sources

To further illustrate the ability of proposed method to study multiscale models, a heat transfer problem is studied as shown in Fig. 22. The conductivity of the model is taken as $K_h = 148\mathrm{W/(m{\cdot}K)}$ and the distances a, b and c are fixed as 9, 7 and 3. Three cooling fins of thickness δ are located on the upper surface of the otherwise square domain, and we

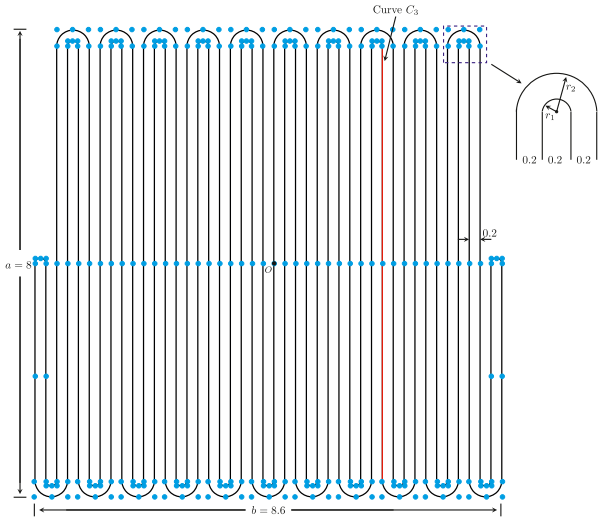

Fig. 19. Heat pipe model.

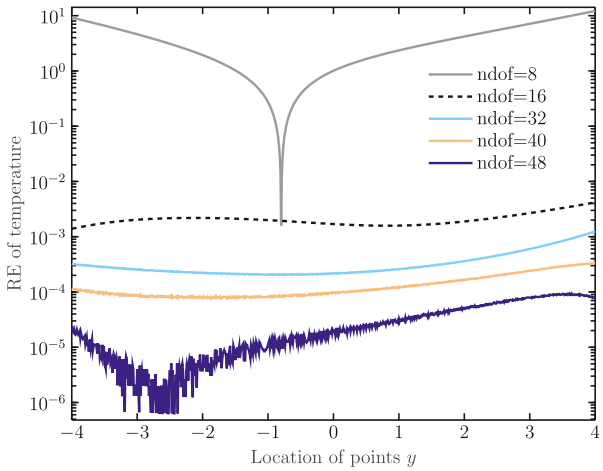

Fig. 20. Relative error of temperature along curve C_3 for different ndofs.

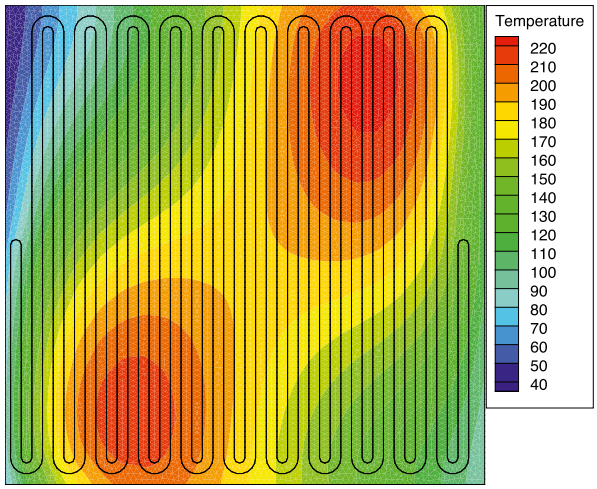

Fig. 21. Temperature distribution inside the matrix for heat lines.

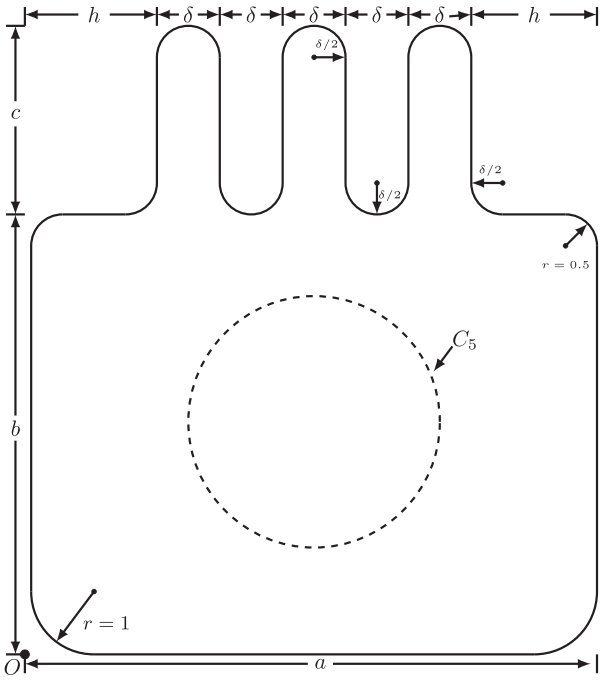

Fig. 22. A multiscale structure.

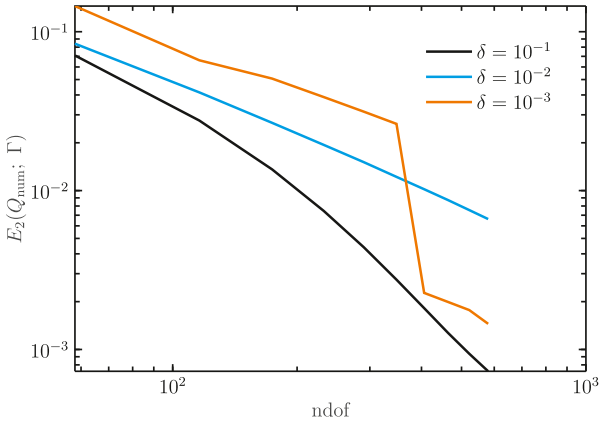

Fig. 23. Convergence of L^2 relative error norm $E_2(Q_{\text{num}};\Gamma)$ with ndof.

consider δ taking values from 1 to 10^{-7}. The dimension $h=(a-6\delta-1)/2$. The temperature on the boundary is prescribed as $T=0.5(x^2-y^2+x+y)$, the origin of the coordinate system being located at point O in Fig. 22.

Fig. 23 shows the convergence of the L^2 relative error norm $E_2(Q_{\text{num}};\Gamma)$ as the number of degrees of freedom (ndof) increases from 58 to 580 with different coating thickness δ. The convergence can be clearly seen. The reason for the fluctuation in relative error norm for $\delta=10^{-3}$ is that in the hybrid scheme the exponential transformation method is now activated. Fig. 24 presents the L^2 relative error norm $E_2(T_{\text{num}};\Omega^{L^2})$ of temperature. As shown in Fig. 22, the considered domain Ω^{L^2} is a circular region with boundary C_5, which is defined as

$$C_5=\{(x,y): x=4.5+r_0\cos(\theta), y=3.5+r_0\sin(\theta), \theta\in(0,2\pi), r_0=1.5\}. \tag{50}$$

The convergence can be clearly seen even when the values of δ reach 10^{-6}. It is evident that both the two methods can produce similar results when $\delta>10^{-2}$. However, when $\delta<10^{-2}$ the results obtained by conventional IGABEM become less satisfactory. The reason for this is that nearly singular integrals appear when δ decreases to 10^{-6}. The proposed scheme can evaluate the nearly singular integrals accurately. Thus, the accuracy of results remains stable.

In Fig. 25, we study the effect of critical aspect ratio d^*_{crit} on the CPU time, the L^2 relative error norm of boundary heat flux $E_2(T_{\text{num}};\Gamma)$ and the domain L^2 relative error norm of inside temperature $E_2(T_{\text{num}};\Omega^{L^2})$. Here, δ is fixed as 10^{-3} and ndof = 174. Fig. 25 shows the CPU time will increase with the reduction of d^*_{crit}. The reason for this is that the adaptive

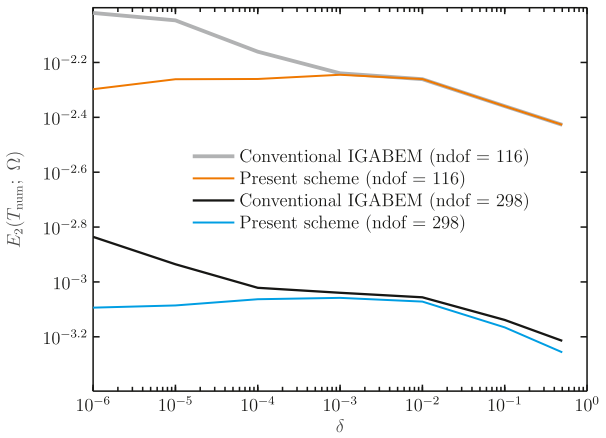

Fig. 24. L^2 relative errors norm $E_2(T_{\text{num}};\Omega^{L^2})$ for different methods.

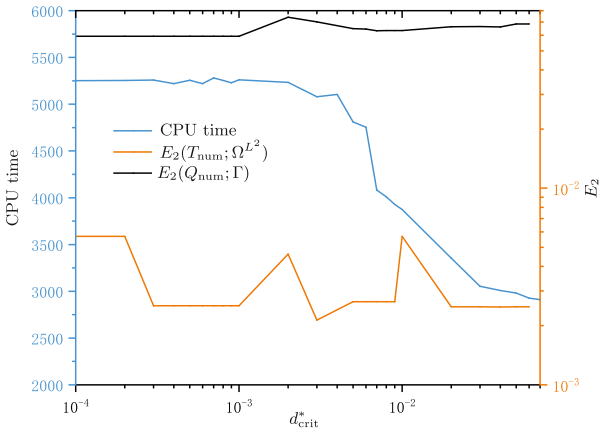

Fig. 25. CPU time and $E_2(T_{\text{num}};\Omega^{L^2})$ with different d^*_{crit}.

integral scheme is used in the hybrid integral method and more sub-knot spans are needed to reach the error tolerance. As in the error analysis, the method consistently delivers very high accuracy for a small d^*_{crit}. In contrast, with the increase of the value of d^*_{crit}, the CPU time will reduce when the values of d^*_{crit} tend to 0.1. The reason for this is the that more nearly singular integrals are computed by the transformation method (fixed number of Gauss points is used).

The numerical temperature distribution inside the substrate when $\delta = 5 \times 10^{-4}$ are given in Figs. 26 and 27. For the two figures, the temperature on the boundary is given as $T = 0.5(x^2 - y^2 + x + y) + 100$. And the heat source $b(x)$ for the two figures are taken as 0 W/m^2 and 100 W/m^2, respectively. Thus, we can find the influence of the heat source on the temperature distribution.

We now introduce a model of a real physical problem and replace the Dirichlet boundaries around the cooling fins with convective boundaries over which a heat transfer coefficient forms part of a convective condition. As shown in Fig. 28, a circular source of radius $R = 2.5$ and having a source strength of $b(x) = 100$ W/m^2 emits heat that will be transmitted to a cooling fluid through the convective boundaries. The bottom, left and right surface temperatures on the bottom, left and right edges of the substrate are prescribed constant at 50°C. The cooling fins on the top side of the substrate is exposed to cooling fluid at a temperature $T_f = 0$ °C, and a heat transfer coefficient of 10 W/m^2·K applies. For this problem, an analytical solution is not available, and the convergence of the problem is established by taking a very refined IGABEM model (with ndof = 960) as the reference solution. Here we will take a detailed look at what is going on in the sharp corner at the base of the cooling fins.

To demonstrate the benefits of the current method, in Fig. 29 we compare the current results (temperatures along C_6 shown in Fig. 28) against a conventional polynomial basis BEM simulation on this model with $\delta = 1$. In Fig. 29, both the current solutions and polynomial basis BEM solutions are obtained by using ndof = 320. A finite element model (with 28043 elements) is constructed with the FEM software ABAQUS to offer a reference solution in this figure. As shown in Fig. 29, the temperature obtained by the current scheme is more accurate than that obtained by BEM based on the conventional shape functions when ndof is the same.

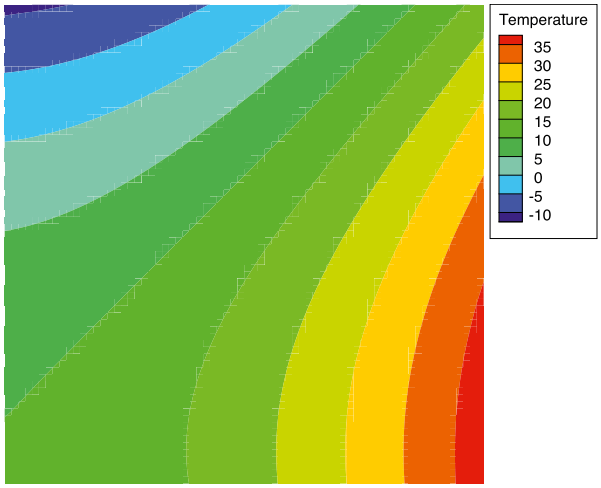

Fig. 26. Temperature distribution inside the matrix.

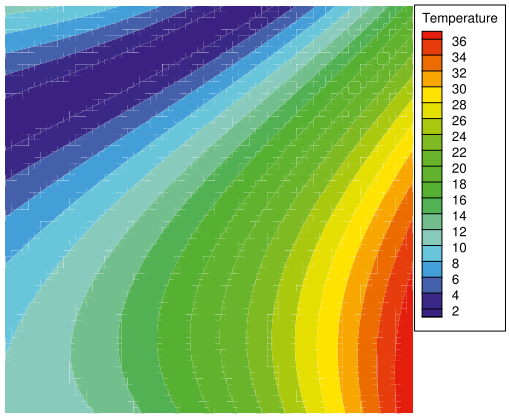

Fig. 27. Temperature distribution inside the matrix with $b(x) = 100$ W/m^2.

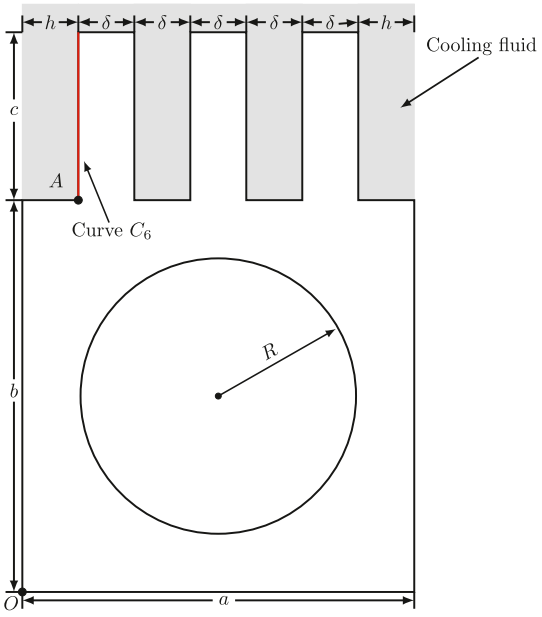

Fig. 28. Convection heat transfer through the multiscale structure.

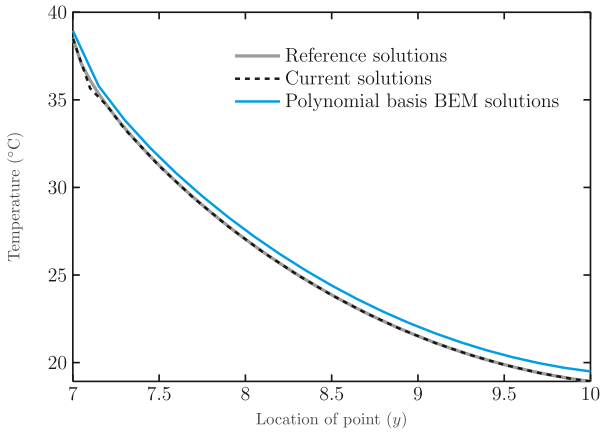

Fig. 29. Temperature distribution at the interface between the cooling fin and cooling fluid for different methods.

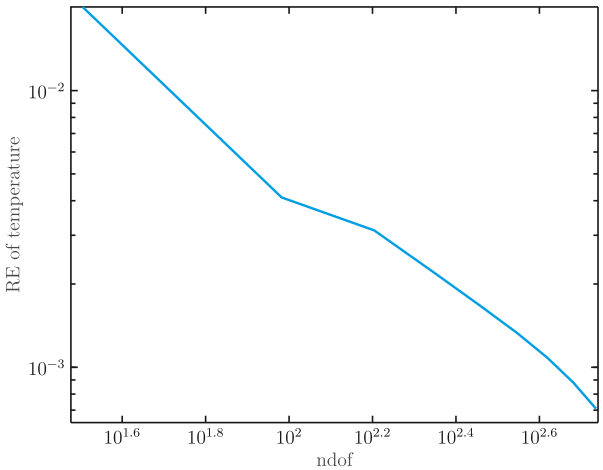

Fig. 30. Temperature convergence.

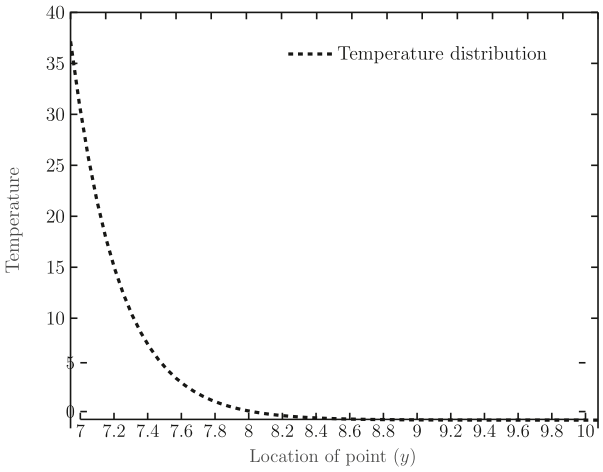

Fig. 31. Temperature distribution along the cooling fins.

It is impossible to obtain an analytical solution for this problem. Therefore, we show the temperature distribution at the interface between the cooling fin and cooling fluid. On one hand we can see the correctness of the results through the trend of temperature variation. On the other hand the temperature at the interface between the cooling fin and cooling fluid is an important indicator of concern to engineers. Fig. 30 shows the temperature convergence at point A (shown in Fig. 28) with coordinates $((7-5\delta)/2, 7)$ when the NURBS is refined. We consider the fins of thickness $\delta = 10^{-2}$. Fig. 31 shows the temperature distribution along the cooling fins, from which we can see that the temperatures drop to 0 °C (the temperature of the cooling fluid) from 37 °C along the cooling fin.

6. Conclusions

In this paper, an IGABEM algorithm has been presented for the thermal analysis of multiscale and complex structures containing arbitrary heat sources. To accurately evaluate the nearly singular integrals caused by the different sizes of isogeometric boundary elements, a hybrid of the adaptive integral and exponential transformation approaches is presented. The exponential transformation method is used in the region very close to the source point, and the adaptive scheme used in the more distant parts of the element. In this way, the nearly singular integrals in the IGABEM for multiscale structures can be evaluated efficiently. The regular integrals for those isogeometric boundary elements with large physical domain are computed by the adaptive integral method, which delivers high accuracy at optimal computational cost by choosing the appropriate number of Gauss points automatically. The radial integration method is used to treat the domain integral due to the arbitrary heat source.

A range of numerical examples collectively demonstrate that the proposed IGABEM formulation will be an efficient method for the study of multiscale structures for electronic packaging problems.

Acknowledgments

The research was supported by the National Natural Science Foundation of China (No. 12002009), the General Program of Science and Technology Development Project of Beijing Municipal Education Commission (No. KM202110005032) and General Program of Science and Technology Development Project of BJUT. The authors thank the editors and reviewers for their valuable comments. The author Yanpeng Gong would also like to thank Qi He of Beijing University of Technology for his excellent meshing work in numerical example 5.2.

References

[1] L. Krambeck, G.A. Bartmeyer, D.O. Souza, D. Fusão, P.H.D. Santos, T. Antonini Alves, Experimental thermal performance of different capillary structures for heat pipes, Energy Eng. 118 (1) (2021) 1–14.
[2] V. Radmard, Y. Hadad, S. Rangarajan, C.H. Hoang, N. Fallahtafti, C.L. Arvin, K. Sikka, S.N. Schiffres, B.G. Sammakia, Multi-objective optimization of a chip-attached micro pin fin liquid cooling system, Appl. Therm. Eng. 195 (2021) 117187.
[3] K. Sharma, R. Mittra, Novel techniques for numerically efficient solution of multiscale problems in computational electromagnetics, Int. J. Numer. Model. Electron. Netw. Devices Fields 33 (2) (2020) e2663.
[4] Y. Shao, Z. Peng, J. Lee, Thermal analysis of high-power integrated circuits and packages using nonconformal domain decomposition method, IEEE Trans. Compon. Packag. Manuf. Technol. 3 (8) (2013) 1321–1331.
[5] T.C. Wang, C.C. Yeh, X. Xu, K.E. Sayed, C.S. Lin, Modeling wafer bending effects on RDL layer reliability in a multiple die package, in: 2018 IEEE International Interconnect Technology Conference (IITC), 2018, pp. 88–90.
[6] T. Hughes, J.A. Cottrell, Y. Bazilevs, Isogeometric analysis: CAD, finite elements, NURBS, exact geometry and mesh refinement, Comput. Methods Appl. Mech. Eng. 194 (39-41) (2005) 4135–4195.
[7] J. López, N. Valizadeh, T. Rabczuk, An isogeometric phase-field based shape and topology optimization for flexoelectric structures, Comput. Methods Appl. Mech. Eng. 391 (2022) 114564.
[8] M. Chasapi, L. Mester, B. Simeon, S. Klinkel, Isogeometric analysis of 3D solids in boundary representation for problems in nonlinear solid mechanics and structural dynamics, Int. J. Numer. Methods Eng. 123 (5) (2022) 1228–1252.
[9] Z. Zou, T. Hughes, M. Scott, D. Miao, R. Sauer, Efficient and robust quadratures for isogeometric analysis: reduced gauss and Gauss–Greville rules, Comput. Methods Appl. Mech. Eng. 392 (2022) 114722.
[10] S. Wang, J. Ren, X. Fang, H. Lin, G. Xu, H. Bao, J. Huang, IGA-suitable planar parameterization with patch structure simplification of closed-form polysquare, Comput. Methods Appl. Mech. Eng. 392 (2022) 114678.
[11] J. Videla, C. Anitescu, T. Khajah, S.P.A. Bordas, E. Atroshchenko, *h*- and *p*-adaptivity driven by recovery and residual-based error estimators for PHT-splines applied to time-harmonic acoustics, Comput. Math. Appl. 77 (9) (2019) 2369–2395.
[12] C. Jansari, J. Videla, S. Natarajan, S.P. Bordas, E. Atroshchenko, Adaptive enriched geometry independent field approximation for 2D time-harmonic acoustics, Comput. Struct. 263 (2022) 106728.
[13] K. Li, T. Yu, T.Q. Bui, Adaptive XIGA shakedown analysis for problems with holes, Eur. J. Mech. A Solids 93 (2022) 104502.
[14] Q. Zang, J. Liu, W. Ye, F. Yang, C. Hao, G. Lin, Static and free vibration analyses of functionally graded plates based on an isogeometric scaled boundary finite element method, Compos. Struct. 288 (2022) 115398.
[15] D. Schillinger, L. Dedé, M.A. Scott, J.A. Evans, M.J. Borden, E. Rank, T.J. Hughes, An isogeometric design-through-analysis methodology based on adaptive hierarchical refinement of NURBS, immersed boundary methods, and T-spline cad surfaces, Comput. Methods Appl. Mech. Eng. 249-252 (2012) 116–150.
[16] R. Jahanbin, S. Rahman, Stochastic isogeometric analysis in linear elasticity, Comput. Methods Appl. Mech. Eng. 364 (2020) 112928.
[17] S. Khakalo, A. Laukkanen, Strain gradient elasto-plasticity model: 3D isogeometric implementation and applications to cellular structures, Comput. Methods Appl. Mech. Eng. 388 (2022) 114225.
[18] S. Nishi, T. Yamada, K. Izui, S. Nishiwaki, K. Terada, Isogeometric topology optimization of anisotropic metamaterials for controlling high-frequency electromagnetic wave, Int. J. Numer. Methods Eng. 121 (6) (2020) 1218–1247.
[19] A. Buffa, G. Sangalli, R. Vázquez, Isogeometric analysis in electromagnetics: B-splines approximation, Comput. Methods Appl. Mech. Eng. 199 (17) (2010) 1143–1152.
[20] A. Simona, L. Bonaventura, C. de Falco, S. Schöps, Isogeometric approximations for electromagnetic problems in axisymmetric domains, Comput. Methods Appl. Mech. Eng. 369 (2020) 113211.

[21] F. Seyfaddini, H. Nguyen-Xuan, V.H. Nguyen, A semi-analytical isogeometric analysis for wave dispersion in functionally graded plates immersed in fluids, Acta Mech. 232 (2021) 1619–6937.
[22] J.A. Rodrigues, Isogeometric analysis for fluid shear stress in cancer cells, Math. Comput. Appl. 25 (2) (2020).
[23] Y. Xue, G. Jin, T. Ye, K. Shi, S. Zhong, C. Yang, Isogeometric analysis for geometric modelling and acoustic attenuation performances of reactive mufflers, Comput. Math. Appl. 79 (12) (2020) 3447–3461.
[24] J. Dölz, H. Harbrecht, C. Jerez-Hanckes, M. Multerer, Isogeometric multilevel quadrature for forward and inverse random acoustic scattering, Comput. Methods Appl. Mech. Eng. 388 (2022) 114242.
[25] E. Zampieri, L.F. Pavarino, Isogeometric collocation discretizations for acoustic wave problems, Comput. Methods Appl. Mech. Eng. 385 (2021) 114047.
[26] V. Agrawal, S.S. Gautam, Varying-order NURBS discretization: an accurate and efficient method for isogeometric analysis of large deformation contact problems, Comput. Methods Appl. Mech. Eng. 367 (2020) 113125.
[27] V.N. Van Do, C.-H. Lee, Isogeometric layerwise formulation for bending and free vibration analysis of laminated composite plates, Acta Mech. 232 (2021) 1619–6937.
[28] F. Bekhoucha, Isogeometric analysis for in-plane free vibration of centrifugally stiffened beams including coriolis effects, Mech. Res. Commun. 111 (2021) 103645.
[29] A. del Toro Llorens, J. Kiendl, An isogeometric finite element-boundary element approach for the vibration analysis of submerged thin-walled structures, Comput. Struct. 256 (2021) 106636.
[30] F. Fathi, L. Chen, R. de Borst, Extended isogeometric analysis for cohesive fracture, Int. J. Numer. Methods Eng. 121 (20) (2020) 4584–4613.
[31] S. Singh, I. Singh, Extended isogeometric analysis for fracture in functionally graded magneto-electro-elastic material, Eng. Fract. Mech. 247 (2021) 107640.
[32] Y. Xia, X. Meng, G. Shen, G. Zheng, P. Hu, Isogeometric analysis of cracks with peridynamics, Comput. Methods Appl. Mech. Eng. 377 (2021) 113700.
[33] F. Fathi, L. Chen, R. de Borst, X-IGALME: isogeometric analysis extended with local maximum entropy for fracture analysis, Int. J. Numer. Methods Eng. 122 (21) (2021) 6103–6125.
[34] F. Fathi, R. de Borst, Geometrically nonlinear extended isogeometric analysis for cohesive fracture with applications to delamination in composites, Finite Elem. Anal. Des. 191 (2021) 103527.
[35] C. Nguyen, X. Zhuang, L. Chamoin, X. Zhao, H. Nguyen-Xuan, T. Rabczuk, Three-dimensional topology optimization of auxetic metamaterial using isogeometric analysis and model order reduction, Comput. Methods Appl. Mech. Eng. 371 (2020) 113306.
[36] J. López, C. Anitescu, T. Rabczuk, Isogeometric structural shape optimization using automatic sensitivity analysis, Appl. Math. Model. 89 (2021) 1004–1024.
[37] K.M. Hamdia, H. Ghasemi, X. Zhuang, T. Rabczuk, Multilevel Monte Carlo method for topology optimization of flexoelectric composites with uncertain material properties, Eng. Anal. Bound. Elem. 134 (2022) 412–418.
[38] T.M. Le, D. Vo, T.Q. Bui, T. Van Huynh, S. Limkatanyu, J. Rungamornrat, Spectral stochastic isogeometric analysis of microbeams with material uncertainty, in: C. Ha-Minh, A.M. Tang, T.Q. Bui, X.H. Vu, D.V.K. Huynh (Eds.), CIGOS 2021, Emerging Technologies and Applications for Green Infrastructure, Springer Singapore, Singapore, 2022, pp. 491–498.
[39] W. Fang, J. Zhang, T. Yu, T.Q. Bui, Analysis of thermal effect on buckling of imperfect FG composite plates by adaptive XIGA, Compos. Struct. 275 (2021) 114450.
[40] T. Hageman, R. de Borst, A refined two-scale model for newtonian and non-newtonian fluids in fractured poroelastic media, J. Comput. Phys. 441 (2021) 110424.
[41] Y. Bazilevs, V.M. Calo, J.A. Cottrell, J.A. Evans, T.J.R. Hughes, S. Lipton, M.A. Scott, T.W. Sederberg, Isogeometric analysis using T-splines, Comput. Methods Appl. Mech. Eng. 199 (5-8) (2010) 229–263.
[42] S. May, J. Vignollet, R.d. Borst, Powell–Sabin B-splines and unstructured standard T-splines for the solution of the Kirchhoff-love plate theory exploiting Bézier extraction, Int. J. Numer. Methods Eng. 107 (3) (2016) 205–233.
[43] X. Xie, A. Yang, N. Jiang, W. Zhao, Z. Liang, S. Wang, Adaptive topology optimization under suitably graded THB-spline refinement and coarsening, Int. J. Numer. Methods Eng. 122 (20) (2021) 5971–5998.
[44] R. de Borst, L. Chen, The role of Bézier extraction in adaptive isogeometric analysis: local refinement and hierarchical refinement, Int. J. Numer. Methods Eng. 113 (6) (2018) 999–1019.
[45] T. Kanduč, C. Giannelli, F. Pelosi, H. Speleers, Adaptive isogeometric analysis with hierarchical box splines, Comput. Methods Appl. Mech. Eng. 316 (2017) 817–838.
[46] L. Chen, B. Li, R.d. Borst, The use of Powell–Sabin B-splines in a higher-order phase-field model for crack kinking, Comput. Mech. 67 (2021) 127–137.
[47] Z. Khatir, S. Lefebvre, Boundary element analysis of thermal fatigue effects on high power IGBT modules, Microelectron. Reliab. 44 (6) (2004) 929–938.
[48] R. Simpson, S. Bordas, J. Trevelyan, T. Rabczuk, A two-dimensional isogeometric boundary element method for elastostatic analysis, Comput. Methods Appl. Mech. Eng. 209-212 (2012) 87–100.
[49] R. Simpson, S. Bordas, H. Lian, J. Trevelyan, An isogeometric boundary element method for elastostatic analysis: 2D implementation aspects, Comput. Struct. 118 (2013) 2–12.
[50] M. Taus, G.J. Rodin, T.J. Hughes, M.A. Scott, Isogeometric boundary element methods and patch tests for linear elastic problems: formulation, numerical integration, and applications, Comput. Methods Appl. Mech. Eng. 357 (2019) 112591.
[51] S. Li, J. Trevelyan, W. Zhang, D. Wang, Accelerating isogeometric boundary element analysis for three-dimensional elastostatics problems through blackbox fast multipole method with proper generalized decomposition, Int. J. Numer. Methods Eng. 114 (9) (2018) 975–998.
[52] Y.H. Wu, C.Y. Dong, H.S. Yang, Isogeometric FE-BE coupling approach for structural-acoustic interaction, J. Sound Vib. 481 (2020) 115436.
[53] C. Xu, C. Dong, RI-IGABEM in inhomogeneous heat conduction problems, Eng. Anal. Bound. Elem. 124 (2021) 221–236.
[54] L.L. Chen, H. Lian, Z. Liu, H.B. Chen, E. Atroshchenko, S. Bordas, Structural shape optimization of three dimensional acoustic problems with isogeometric boundary element methods, Comput. Methods Appl. Mech. Eng. 355 (Oct.1) (2019) 926–951.
[55] L. Chen, C. Lu, H. Lian, Z. Liu, S. Bordas, Acoustic topology optimization of sound absorbing materials directly from subdivision surfaces with isogeometric boundary element methods, Comput. Methods Appl. Mech. Eng. 362 (2020) 112806.
[56] H.L. Oliveira, H. Andrade, E.D. Leonel, An isogeometric boundary element approach for topology optimization using the level set method, Appl. Math. Model. 84 (2020) 536–553.
[57] K.V. Kostas, M.M. Fyrillas, C.G. Politis, A.I. Ginnis, P.D. Kaklis, Shape optimization of conductive-media interfaces using an IGA - BEM solver, Comput. Methods Appl. Mech. Eng. 340 (OCT.1) (2018) 600–614.
[58] W. Wang, Q. Zang, Z. Wei, Z. Guo, An isogeometric boundary element method for liquid sloshing in the horizontal eccentric annular tanks with multiple porous baffles, Ocean Eng. 189 (2019) 106367.
[59] Z. Han, C. Cheng, S. Yao, Z. Niu, Determination of stress intensity factors of V - notch structures by characteristic analysis coupled with isogeometric boundary element method, Eng. Fract. Mech. 222 (2019) 106717.
[60] F.L. Sun, C.Y. Dong, H.S. Yang, Isogeometric boundary element method for crack propagation based on Bezier extraction of NURBS, Eng. Anal. Bound. Elem. 99 (FEB) (2019) 76–88.
[61] G. Beer, C. Duenser, Isogeometric boundary element analysis of problems in potential flow, Comput. Methods Appl. Mech. Eng. 347 (APR.15) (2019) 517–532.
[62] G. Beer, C. Duenser, Advanced 3-D boundary element analysis of underground excavations, Comput. Geotech. 101 (SEP) (2018) 196–207.
[63] H. Yu, Y. Guo, Y. Gong, F. Qin, Thermal analysis of electronic packaging structure using isogeometric boundary element method, Eng. Anal. Bound. Elem. 128 (2021) 195–202.

[64] Y. Gu, X. He, W. Chen, C. Zhang, Analysis of three-dimensional anisotropic heat conduction problems on thin domains using an advanced boundary element method, Comput. Math. Appl. 75 (1) (2018) 33–44.
[65] Y. Gong, C. Dong, Y. Bai, Evaluation of nearly singular integrals in isogeometric boundary element method, Eng. Anal. Bound. Elem. 75 (2017) 21–35.
[66] S. Keuchel, N.C. Hagelstein, O. Zaleski, O. von Estorff, Evaluation of hypersingular and nearly singular integrals in the isogeometric boundary element method for acoustics, Comput. Methods Appl. Mech. Eng. 325 (2017) 488–504.
[67] Z. Han, Y. Huang, C. Cheng, Y. Liang, Z. Hu, Z. Niu, The semianalytical analysis of nearly singular integrals in 2D potential problem by isogeometric boundary element method, Int. J. Numer. Methods Eng. 121 (16) (2020) 3560–3583.
[68] Y. Gong, J. Trevelyan, G. Hattori, C. Dong, Hybrid nearly singular integration for isogeometric boundary element analysis of coatings and other thin 2D structures, Comput. Methods Appl. Mech. Eng. 346 (2019) 642–673.
[69] Y. Gong, C. Dong, F. Qin, G. Hattori, J. Trevelyan, Hybrid nearly singular integration for three-dimensional isogeometric boundary element analysis of coatings and other thin structures, Comput. Methods Appl. Mech. Eng. 367 (2020) 113099.
[70] X. Gao, T.G. Davies, Adaptive integration in elastolastic boundary element analysis, J. Chin. Inst. Eng. 23 (3) (2000) 349–356.
[71] Y.P. Gong, C.Y. Dong, An isogeometric boundary element method using adaptive integral method for 3D potential problems, J. Comput. Appl. Math. 319 (2017) 141–158.
[72] S. Bu, T.G. Davies, Effective evaluation of non-singular integrals in 3D BEM, Adv. Eng. Softw. 23 (2) (1995) 121–128.
[73] C. Wang, X.-J. Huang, K. Vafai, Analysis of hotspots and cooling strategy for multilayer three-dimensional integrated circuits, Appl. Therm. Eng. 186 (2021) 116336.
[74] C. Dong, S. Lo, Y. Cheung, Application of the boundary-domain integral equation in elastic inclusion problems, Eng. Anal. Bound. Elem. 26 (6) (2002) 471–477.
[75] D. Nardini, C. Brebbia, A new approach to free vibration analysis using boundary elements, Appl. Math. Model. 7 (3) (1983) 157–162.
[76] A.C. Neves, C.A. Brebbia, The multiple reciprocity boundary element method in elasticity: a new approach for transforming domain integrals to the boundary, Int. J. Numer. Methods Eng. 31 (4) (1991) 709–727.
[77] X.W. Gao, A boundary element method without internal cells for two-dimensional and three-dimensional elastoplastic problems, J. Appl. Mech., Trans. ASME 69 (2) (2002) 154–160.
[78] X.-W. Gao, Boundary element analysis in thermoelasticity with and without internal cells, Int. J. Numer. Methods Eng. 57 (7) (2003) 975–990.
[79] Y. Gong, C. Dong, X. Qin, An isogeometric boundary element method for three dimensional potential problems, J. Comput. Appl. Math. 313 (2017) 454–468.
[80] Y. Gong, C. Dong, X. Qu, An adaptive isogeometric boundary element method for predicting the effective thermal conductivity of steady state heterogeneity, Adv. Eng. Softw. 119 (2018) 103–115.
[81] Y.M. Zhang, Y. Gu, J.T. Chen, Boundary layer effect in BEM with high order geometry elements using transformation, Comput. Model. Eng. Sci. 45 (3) (2009) 227–247.
[82] X. Qin, J. Zhang, G. Xie, F. Zhou, G. Li, A general algorithm for the numerical evaluation of nearly singular integrals on 3D boundary element, J. Comput. Appl. Math. 234 (14) (2011) 4174–4186.
[83] G. Xie, F. Zhou, J. Zhang, X. Zheng, C. Huang, New variable transformations for evaluating nearly singular integrals in 3D boundary element method, Eng. Anal. Bound. Elem. 37 (9) (2013) 1169–1178.
[84] Y.-J. Jia, F. Xiao, Y.-Q. Duan, Y.-F. Luo, B.-L. Liu, Y.-L. Huang, Modeling method for electrothermal cosimulation of high-power IGBT, IEEJ Trans. Electr. Electron. Eng. 14 (11) (2019) 1711–1718.